Draft version January 27, 2022
Typeset using LaTeX **twocolumn** style in AASTeX631

AGN Selection Methods Have Profound Impacts on the Distributions of Host Galaxy Properties

Zhiyuan Ji,[1] Mauro Giavalisco,[1] Allison Kirkpatrick,[2] Dale Kocevski,[3] Emanuele Daddi,[4] Ivan Delvecchio,[5] and Cassandra Hatcher[2]

[1] *University of Massachusetts Amherst, 710 North Pleasant Street, Amherst, MA 01003-9305, USA*
[2] *Department of Physics & Astronomy, University of Kansas, Lawrence, KS 66045, USA*
[3] *Department of Physics and Astronomy, Colby College, Waterville, ME 04961, USA*
[4] *CEA, Irfu, DAp, AIM, Université Paris-Saclay, Université de Paris, CNRS, F-91191 Gif-sur-Yvette, France*
[5] *INAF - Osservatorio Astronomico di Brera, via Brera 28, I-20121, Milano, Italy*

ABSTRACT

We present a comparative study of X-ray and IR AGNs at $z \approx 2$ to highlight the important AGN selection effects on the distributions of host galaxy properties. Compared with non-AGN star-forming galaxies (SFGs) on the main sequence, X-ray AGNs have similar median star formation (SF) properties, but their incidence (q_{AGN}) is higher among galaxies with either enhanced or suppressed SF, and among galaxies with larger stellar mass surface density, regardless if it is measured within half-light radius (Σ_e) or central 1kpc (Σ_{1kpc}). Unlike X-ray AGNs, IR AGNs are less massive, and have enhanced SF and similar distributions of colors, Σ_e and Σ_{1kpc} relative to non-AGN SFGs. Given that Σ_e and Σ_{1kpc} strongly correlate with M_*, we introduce the fractional mass within central 1kpc ($\frac{M_{1kpc}}{M_*}$), which only *weakly* depends on M_*, to quantify galaxy compactness. Both AGN populations have similar $\frac{M_{1kpc}}{M_*}$ distributions compared to non-AGN SFGs'. While q_{AGN} increases with Σ_e and Σ_{1kpc}, it remains constant with $\frac{M_{1kpc}}{M_*}$, indicating that the trend of increasing q_{AGN} with Σ is driven by M_* more than morphology. While our findings are not in conflict with the scenario of AGN quenching, they do not imply it either, because the incidence of AGNs hosted in transitional galaxies depends crucially on AGN selections. Additionally, despite the relatively large uncertainty of AGN bolometric luminosities, their very weak correlation, if any, with SF activities, regardless of AGN selections, also argues against a direct causal link between the presences of AGNs and the quenching of massive galaxies at $z \sim 2$.

Keywords: galaxies: evolution – galaxies: formation – galaxies: high-redshift – galaxies: structure

1. INTRODUCTION

Modern observational cosmology, primarily the observations of cosmic large-scale structures such as the Baryon Acoustic Oscillations (e.g. Eisenstein et al. 2005) and the polarization of the Cosmic Microwave Background (e.g. Planck Collaboration et al. 2016), are, for the most part, in good quantitative agreement with the predictions of the Lambda Cold Dark Matter (ΛCDM) paradigm. However, a key prediction of the theory – the mass function of dark matter halos – significantly differs from the observed galaxy stellar mass function at both the low-mass and high-mass ends (see Wechsler & Tinker 2018 and references therein), which reflects the complex, and still poorly-understood, dependence of the physics of star formation on the halo mass and the environment.

In order to reproduce the observations at the high-mass end, a crucial ingredient required by most theoretical models (see Somerville & Davé 2015 and references therein) is the so-called AGN feedback, which refers to the effects produced by the active nucleus activities (winds, jets, radiation) of a massive galaxy on the surrounding interstellar medium (ISM) and circum-galactic medium (CGM). The concept of AGN feedback was initially introduced by Silk & Rees (1998) and Haehnelt et al. (1998) to explain the observed tight correlations among black hole mass (M_{BH}), bulge mass/luminosity and velocity dispersion. Recently, depending on the nature of energy output, two major modes of AGN

Corresponding author: Zhiyuan Ji
zhiyuanji@astro.umass.edu

feedback are being considered: radiative and kinetic feedback (see the review of Fabian 2012 and references therein). Kinetic mode, sometimes also known as radio mode, refers to the feedback effects generated by the mechanical energy of radio jets which are often observed when AGN radiative activities are operating at low levels. In contrast, radiative mode refers to the feedback effects occurring when AGNs are very luminous. In this work, we will specifically focus on the radiative AGNs.

In the absence of AGN feedback, cosmological simulations under the ΛCDM paradigm produce too many massive galaxies compared to the observations (e.g. Oppenheimer et al. 2010; Kaviraj et al. 2017) and, the simulated massive galaxies also are too blue (e.g. Hatton et al. 2003) and too compact (e.g. Peirani et al. 2017). For the simulations, one resolution to those discrepancies is to add the sub-grid AGN feedback models to suppress star formation in massive galaxies, a process generically referred to as AGN quenching. While including such models has become increasingly popular in modern cosmological simulations, a big concern is the large uncertainty on how to properly implement AGN physics and couple the feedback effects to the ISM (e.g. Di Matteo et al. 2005; Booth & Schaye 2009; Weinberger et al. 2017). It is therefore of great importance to observationally investigate the effects of AGNs on the host galaxies.

Taking advantage of deep and high-angular resolution X-ray observations, significant progress has been recently made in understanding the relationship between X-ray AGNs (e.g. Xue et al. 2016; Luo et al. 2017; Fornasini et al. 2018; Brown et al. 2019) and the properties of their host galaxies (e.g. Xue et al. 2010; Yang et al. 2017, 2018; Kocevski et al. 2017). Yet, observational evidence of the feedback effects from X-ray AGNs is far from conclusive. For example, at $z \approx 2$, where both the quasar activities (Hasinger et al. 2005) and cosmic star formation rate density (Madau & Dickinson 2014) peak, AGN feedback (if any) is expected to be strong. A number of studies have been carried out to investigate the star formation properties for the host galaxies of X-ray AGNs out to z∼3 (e.g. Lutz et al. 2010; Santini et al. 2012; Rosario et al. 2012; Rovilos et al. 2012; Page et al. 2012; Harrison et al. 2012; Barger et al. 2015; Hatziminaoglou et al. 2010; Harrison et al. 2012; Stanley et al. 2015; Barger et al. 2019). While many of these studies have consistently shown that the median star formation intensity in galaxies hosting moderate luminous X-ray AGNs ($42 < LogL_X < 44$) is similar to that in normal SFGs, diverging conclusions emerge in luminous ($LogL_X > 44$) X-ray AGN hosts. For example, using far-infrared (FIR) luminosity as the star formation rate estimator, some groups (e.g. Page et al. 2012; Barger et al. 2015) reported suppressed star formation in luminous X-ray AGN hosting galaxies, while others (e.g. Lutz et al. 2010; Santini et al. 2012; Rovilos et al. 2012) reached the opposite conclusion that their samples of luminous X-ray AGNs show enhanced star formation. Yet, other investigators (Harrison et al. 2012; Stanley et al. 2015) reported no dependence of star formation activity on the X-ray AGN luminosity.

One general issue for the observational studies of the effects of the AGN presences on hosting galaxy properties is the interpretation of the data. Empirically speaking, compared with non-AGNs, any distinct distribution of physical properties of AGN hosts can be attributed to the presences of AGNs. However, such attribution does not necessarily imply a causal relationship in the sense that the real cause(s) behind might be some other mechanisms which are also likely to trigger AGN activities, even if the latter is only weakly related, if any, to the properties of the host. One example is galaxy major merger, where strong gravitational torques induced by the merging galaxy/galaxies can drive gas to the center which as a result can simultaneously (1) make the gas distribution more nucleated; (2) trigger a central starburst and increase galactic wide star formation rate and (3) trigger a bright AGN (e.g. Mihos & Hernquist 1996; Sanders et al. 1988; Hopkins et al. 2006).

The other issue comes from the AGN selection, which is the focus of this work. While selecting AGNs in X-ray has been shown to be one of the most efficient ways to study them, it is by no mean complete. Since X-ray photons (soft ones in particular) heavily suffer from the line-of-sight obscuration, X-ray selection itself can miss a significant fraction of obscured AGNs (e.g. Gilli et al. 2007), which become increasingly important at higher redshifts where the fraction of obscured AGNs becomes larger (e.g. Liu et al. 2017). To get a comprehensive observational picture of AGN feedback, the missing population of AGNs must be taken into account.

Observations at mid-IR (MIR) are efficient to identify those highly-obscured AGNs missed by the X-ray selection (e.g. Daddi et al. 2007; Donley et al. 2008), because MIR directly probes the re-processed radiation from the absorbed X-ray, UV and optical photons. The primary issue of studying AGNs in MIR is the confusion with light from the host galaxies. Unless the AGNs are powerful enough, their spectral energy distribution (SED) in MIR is always a comparable mixture of the reprocessed emission from AGNs and the emission from star formations. Despite that the shape of AGN MIR spectra remains to be characterized in details by future studies, e.g. with JWST (e.g. Kirkpatrick et al. 2017),

Field	Parent sample	X-ray AGN	IR AGN
GOODS-S	2500	164	69
GOODS-N	2309	74	69
All	4809	238	138

Table 1. The number of galaxies in each sample.

substantial progress has been recently made in identifying IR AGNs using the broad band photometry in MIR, including the selection methods based on *Spitzer* IRAC colors (e.g. Lacy et al. 2004; Stern et al. 2005; Donley et al. 2008, 2012; Kirkpatrick et al. 2013), *WISE* colors (e.g. Eisenhardt et al. 2012; Stern et al. 2012)) and SED decomposition techniques (e.g. Armus et al. 2007; Pope et al. 2008; Kirkpatrick et al. 2012; Berta et al. 2013). Finally, some progress has also been made in understanding the MIR spectroscopic properties of AGNs at high redshifts using the observations from *Spitzer*/IRS (Kirkpatrick et al. 2013), although such studies are only limited to the luminous AGNs given the MIR sensitivities of current instruments.

In this work, we present a comparative study of the properties of the host galaxies of X-ray- and IR-selected AGNs. Specifically, we will compare the star-formation and morphological properties of the AGN and the non-AGN hosting galaxies, focusing on the effects, if any, of the presences of AGNs on their host galaxies. Throughout this paper, we adopt a ΛCDM cosmology with $\Omega_m = 0.3$, $\Omega_\Lambda = 0.7$ and $h = H_0/(100 kms^{-1}Mpc^{-1}) = 0.7$.

2. SAMPLE SELECTION

In this Section, we describe in details about the sample selections in this work. Table 1 lists the number of galaxies in each sample.

2.1. *Parent Sample*

Our parent sample is the same as that of Lee et al. (2018), which is drawn from *Hubble Space Telescope* (*HST*) H_{160}-band selected 4809 galaxies in the GOODS-S (2500 galaxies) and GOODS-N (2309 galaxies) fields. Both fields have the deep *HST*/ACS data acquired during the GOODS survey (Giavalisco et al. 2004) and the deep *HST*/WFC3 data acquired during the CANDELS survey (Grogin et al. 2011; Koekemoer et al. 2011). The sample galaxies are selected to be in the redshift range of $1.2 < z < 4$ with $M_* > 10^{9.5} M_\odot$ and their isophotal H_{160} signal-to-noise ratios (SNRs) are required to be SNR > 10 in order to get good photometry and hence high-quality photometric redshifts (photo-z) and spectral energy distribution (SED) fitting measures. The full sample is divided into two subsamples according to star formation properties of the galaxies (Figure 1). Star-

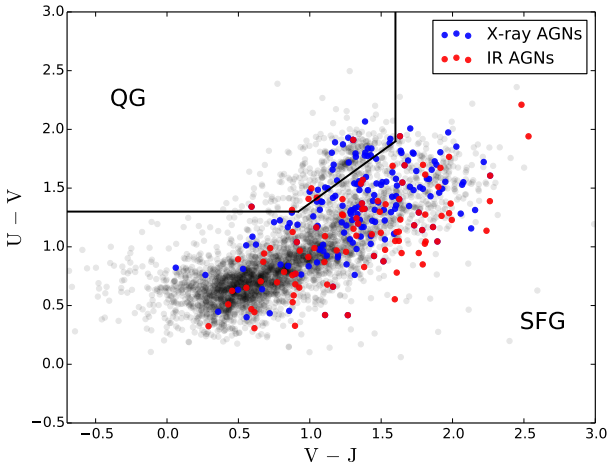

Figure 1. Rest-frame UVJ-color diagram. Black dots are galaxies in the parent sample. Black solid lines mark the boundaries used to separate SFGs and QGs, where QGs are in the region with $U - V > 0.88 (V - J) + 0.49$, $U - V > 1.3$ and $V - J < 1.6$. Overplotted blue and red dots are galaxies identified as X-ray AGNs and IR AGNs respectively (see Section 2.2 and 2.3 for details).

forming galaxies (SFGs) and quiescent galaxies (QGs) are distinguished using the rest-frame UVJ-color diagram (see Section 3.1 for the measurements of rest-frame colors) that was initially proposed by Williams et al. (2009). In this work, we adopt the SFG-QG separation boundary from Schreiber et al. (2015) which is built upon CANDELS galaxies and has been demonstrated to be valid up to $z = 4$. Ji et al. (2018) used the simulation done by Guo et al. (2013) to show that the parent sample is ≈ 80% complete down to $10^9 M_\odot$. In this work, we decide to ignore galaxies with stellar mass less than $10^{9.5} M_\odot$ because (1) a lower-mass galaxy statistically tends to have a lower metallicity (e.g. Tremonti et al. 2004) such that the AGN selection based on IR colors can mimic an AGN when really there is none (Satyapal et al. 2014; Hainline et al. 2016; Marleau et al. 2017; Kaviraj et al. 2019) and (2) it is hard for a $< 10^{9.5} M_\odot$ galaxy's black hole to accrete actively enough to become an AGN from a theoretical point of view (e.g. Fontanot et al. 2011).

2.2. *X-ray AGNs*

The identifications of X-ray AGNs are done by spatially cross-matching the CANDELS catalog of the parent sample with the AGN catalogs of the 7Ms *Chandra* Deep Field South (CDF-S, Luo et al. 2017) and the 2Ms *Chandra* Deep Field North (CDF-N, Xue et al.

2016). Details of AGN classifications in both fields can be found in Xue et al. (2016) and Luo et al. (2017). In short, an X-ray source is classified as an AGN if it meets the criteria built upon intrinsic X-ray luminosity threshold and spectral shape (hardness ratio), as well as the flux ratio between X-ray and other bands (optical, IR and radio). We cross-match the coordinates of the parent sample (H_{160} coordinates from the CANDELS catalog) with X-ray AGNs using a 0.5" radius, the same matching radius has also been used in other works (e.g. Yang et al. 2017, 2018). We have checked that our results do not change if we use a smaller (0.3", 0.4") or larger (0.6", 0.7") radius. To further secure the cross-matching, we request the redshifts of sample galaxies ($z_{\rm CANDELS}$) and those assigned to the matched X-ray counterparts ($z_{\rm Xray}$) are either the same if spectroscopic redshifts are available or within 10% difference (i.e. $|z_{\rm Xray} - z_{\rm CANDELS}|/z_{\rm CANDELS} \leq 10\%$) if photo-z are used. The 10% tolerance of photo-z difference is because of the different photo-z catalogs used in Luo et al. (2017) and Lee et al. (2018). We have checked that our results do not change if we set the tolerance to be 5% or 15%. With a 0.5" matching radius and 10% tolerance of the photo-z difference, we find that 238 galaxies in the parent sample have X-ray AGNs (no duplicated match).

It is worth pointing out that the approach of searching for counterpart within a small radius is not ideal for faint galaxies, given both the centroid errors of X-ray sources and sometimes high background optical/NIR source density. An alternative approach is to use the likelihood-ratio method which has been carried out in both fields (see Section 2.3.3 in Xue et al. 2016 and Section 4.2 in Luo et al. 2017 for details). We have checked, by comparing the 238 cross-matched X-ray AGNs with the counterparts identified using the likelihood-ratio technique, the two matching results are the same, which is not surprising given that the parent sample are relatively bright (recall that we require all galaxies have SNR > 10 in H_{160}) and the addition redshift difference tolerance can further secure our cross matching.

2.3. *IR AGNs*

Because of the availability of deep *Spitzer*/IRAC photometry in the GOODS fields, IR AGNs are selected using the IRAC color-color diagram from Donley et al. (2012), which was built on a large sample of galaxies in the COSMOS field. This selection is able to effectively identify IR AGNs at high redshifts, which has been demonstrated by many other surveys where IRAC photometry is available (e.g. Mendez et al. 2016; Delvecchio et al. 2017; Leung et al. 2017; Donley et al. 2018).

Two IRAC colors are used to select IR AGNs, namely $x = \mathrm{Log}(S_{5.8}/S_{3.6})$ and $y = \mathrm{Log}(S_{8.0}/S_{4.5})$. A galaxy is classified to be an IR AGN host if it meets the following criteria:

$$\begin{cases} 1.21x - 0.27 \leq y \leq 1.21x + 0.27 \\ x \geq 0.08 \\ y \geq 0.15 \\ S_8 > S_{5.8} > S_{4.5} > S_{3.6} \end{cases} \quad (1)$$

$$\begin{cases} z \geq 2.7 \\ x/y \leq 0.95 \\ \mathrm{Log}\, S_8/S_{3.6} \geq \begin{cases} 0.39z - 0.69 & if\ z = 2.7 - 3.1 \\ 0.18z - 0.04 & if\ z = 3.1 - 4.0 \end{cases} \end{cases} \quad (2)$$

Black solid lines in Figure 2 form the boxy region defined by the first three equations of criterion (1). Galaxies within it have AGN-like SEDs (see Figure 2 of Donley et al. 2012), which has further been confirmed by Kirkpatrick et al. (2013) for a sample of 24 μm-selected $0.5< z <4$ galaxies with deep *Spitzer*/IRS spectroscopy. The stellar bump ($\approx 1.6\mu m$) of normal galaxies at $z > 2$ are redshifted into the IRAC 4.5, 5.8 and 8 μm bands, which can effectively contaminate the IR AGN selection. To overcome this, the fourth equation of criterion (1) therefore is required to exclude galaxies in the boxy region with non-monotonically rising SEDs. For galaxies at $z > 2.7$, the additional criterion is required given that the contamination becomes even worse because the stellar light might dominate all IRAC bands. With the additional criterion (2), Donley et al. (2012) showed that it can effective exclude (1) galaxies whose spectral shapes in IRAC four bands are consistent with the rest-frame 1.6 μm stellar bump (the 2nd equation) and (2) galaxies which can be possibly fit by the reddest LIRG/ULIRG templates of Rieke et al. (2009) (the 3rd equation).

With the selection described above, we find 138 IR AGNs, among which 45 ($\approx$ 33%, similar percentage (27%) as found by Delvecchio et al. 2017) are also identified as X-ray AGNs. As demonstrated by Kirkpatrick et al. (2013), the IRAC color selection can miss a fraction of MIR spectroscopically confirmed AGNs which can be better recovered by adding *Spitzer*/MIPS 24 μm and far-infrared (FIR) *Herschel*/PACS 100 μm and SPIRE 250 μm photometry to the selection. Due to the sensitivity and angular resolution of MIR and FIR observations, unfortunately, only $\approx$ 14% of galaxies in the parent sample simultaneously have 24 μm and 100/250 μm photometry. We have checked, among the 46 galax-

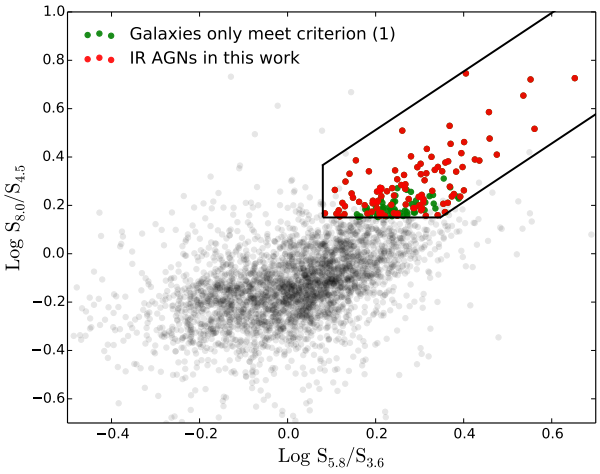

Figure 2. IR AGNs selected by the IRAC color-color diagram of Donley et al. (2012). The red dots are the final IR AGNs, while the green dots are galaxies which only pass criterion (1). The black solid lines mark the region enclosed by the first three equations of criterion (1). Note that there are still a small number of grey points in this region, those are galaxies whose fluxes in IRAC four bands are *not* monotonically increasing (i.e. do not pass the fourth equation of criterion (1)). The details of the selection method can be found in Section 2.3.

ies which are selected as IR AGNs using the selection criteria of Kirkpatrick et al. (2013), 39 of them have already been picked up by our IRAC color selection.

3. MEASUREMENTS & DATA ANALYSIS

3.1. *SED fitting*

Physical parameters, including M_*, star formation rate (SFR) and rest-frame colors, are derived via SED fitting. In the following, we detail the fitting procedure and outline the systematics of the measurements.

Throughout this work, we adopt the SED fitting results of Lee et al. (2018) (hereafter, Lee2018), which uses the Bruzual & Charlot (2003) stellar population synthesis code, assumes a Chabrier (2003) initial mass function (IMF), fixed solar metallicity and the Calzetti et al. (2000) dust attenuation law. Lee2018 takes advantage of the deep CANDELS multi-wavelength photometry that covers from the rest-frame UV to FIR and the official CANDELS photometric redshift catalog (see Dahlen et al. 2013; Hsu et al. 2014) where full probability density functions are used in the determination of photometric redshift. A key feature of the Lee2018 SED modeling approach is that the fitting procedure applies an advanced Monte Carlo Markov Chain algorithm to treat star formation history (SFH) as a free parameter during the fits. In Lee2018, using mock observations derived from semi-analytical models of galaxy evolution, it has been demonstrated that their measurements of M_*, SFR and luminosity-weighted stellar age are much more robust than those derived by setting the functional form of SFH to a pre-assigned type.

A concern of using the Lee2018 measurements, in particular for the AGN hosts, is the ignorance of the AGN contribution during the SED fitting. To check these systematics, we have run another set of SED fitting using SED3FIT (Berta et al. 2013) where the AGN component is included to the modeling. We refer readers to Appendix A for a detailed analysis for the uncertainty of individual parameters derived in this way. In short, the comparisons between Lee2018 and SED3FIT results suggest that, when averaged on the galaxy mix of our sample, neglecting the AGN component in SED modeling

- statistically does not affect the M_* measurement in a significant way, although we do find that properly including AGN contribution is crucial for the M_* measurement of broad line AGNs (BL AGNs). BL AGNs however are a very small fraction ($\approx$5%) of the entire AGN sample and we have checked that our results are insensitive to including/excluding them.

- can lead to an $\approx$ 0.1 dex overestimation of SFRs for the AGN hosts. This systematics will be taken into account in the following discussions with regard to the star formation properties of the AGN hosts.

- statistically does not significantly affect the measurement of rest-frame apparent (dust-attenuated) colors U$-$V and V$-$J, and dust-corrected colors $(U-V)_{corr}$ and $(V-J)_{corr}$. We also notice that the scatter of the $(V-J)_{corr}$ measurement is slightly larger in IR AGNs than X-ray AGNs and non-AGNs, which is likely due to the generally larger AGN contribution to the J band in IR AGN hosts.

While the SED3FIT tests reveal some tensions of using Lee2018 measurements for AGN hosts (BL AGNs in particular), fortunately, the rather tight correlations between the parameters derived from the two SED fittings (see Figures in Appendix A) suggests that the overall determination of the parameters that we have considered is *insensitive* to the inclusion of the AGN component. Quantifying systematic differences among different SED fitting procedures to a finer degree of accuracy is be-

yond the scope of this work. We decide to use Lee2018 measurements because parts of the following discussions rely on the measurement of properties of galaxies on the star-forming main sequence, which has been carefully done for the parent sample of Lee2018. Using different SED fitting algorithms and assumptions for AGNs and non-AGNs might introduce systematic bias owing to the systematic shifts in the measurements of M_* and SFR (see Appendix A and also other works like Leja et al. 2019) that, as small or rare as they are, we prefer to avoid.

In addition to comparing with Lee2018 measurements, running SED3FIT also helps us validate our IRAC color selection method, as well as quantify AGN luminosity for the IR AGNs (see Section 4.1.2 for details). Figure 3 shows the best-fit SEDs of X-ray and IR AGNs derived by SED3FIT. Significant AGN contribution to MIR flux is seen in IR AGNs, illustrating the good agreement between the results from the SED decomposition and the adopted IRAC color selection (Section 2.3). The Figure also shows that identifying AGNs at MIR wavelength can sometimes be hard when galaxy stellar SED dominates the total light in the optical/IR part of the spectrum despite the clear presence of the AGN at X-ray wavelengths, which again highlights the importance of selecting AGNs in more than one wavelength range, as we have already discussed in Section 1. Figure 4 further shows the distribution of the ratio of AGN IR luminosity divided by total rest $5-10\mu$m IR luminosity ($f_{AGN}^{5-10\mu\mathrm{m}}$). Like those seen in the best-fit SEDs, the IR AGNs have much higher contribution to MIR flux than the X-ray AGNs.

3.2. *Morphological measurements*

Morphological properties of the AGN hosts and normal galaxies are derived by fitting the CANDELS H_{160} images with 2-dimensional (2D) light profiles using GALFIT (Peng et al. 2010). Key morphological parameters that we are interested in are: effective radius (R_e, a.k.a half light radius), Sérsic index (n), stellar mass surface density within effective radius (Σ_e), stellar mass surface density within central 1 kpc ($\Sigma_{1\mathrm{kpc}}$) and fractional mass within central 1 kpc ($\frac{M_{1\mathrm{kpc}}}{M_*}$). In the following, we will first introduce the basic setup of GALFIT and then describe in details on how we measure the aforementioned morphological parameters and their uncertainties. We will also test the validity of the assumed 2D light profile model and discuss the relevant systematics. We will finally describe in details on our purposes and advantages of using $\frac{M_{1\mathrm{kpc}}}{M_*}$ to quantify galaxy compactness.

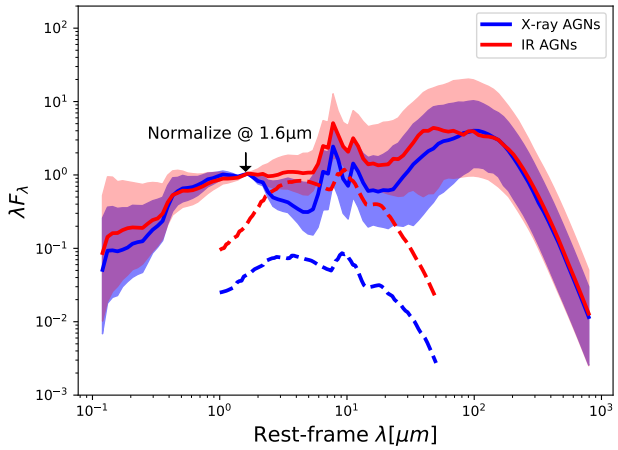

Figure 3. SED3FIT-derived SEDs of X-ray (blue) and IR (red) AGN hosts. Each best-fit model is normalized to the rest-frame 1.6μm. Solid lines show the medians and shaded regions show the 16th-84th percentile ranges. The dashed lines show the median AGN contributions.

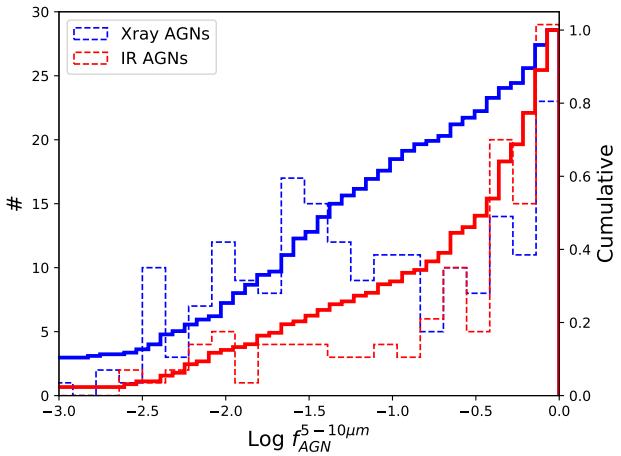

Figure 4. SED3FIT-derived AGN contributions to rest $5-10\mu m$ IR luminosity ($L_{AGN}^{5-10\mu m}/L_{Total}^{5-10\mu m} = f_{AGN}^{5-10\mu m}$). Blue and red dashed histograms show the distribution of X-ray and IR AGNs respectively. Corresponding cumulative distributions are shown as solid lines.

3.2.1. GALFIT *fittings and parameter uncertainties*

Before running GALFIT, we center on each sample galaxy to make a 6"×6" cutout. We adopt the H_{160} point spread function (PSF) from the CANDELS team (van der Wel et al. 2012). To get rid of the isophotes contamination from the neighboring galaxies, we first find all galaxies in the cutout image with the aid of

the CANDELS H_{160} segmentation map. Then, rather than fitting the neighboring galaxies, we fix and model their light profiles using the best-fit 2D Sérsic profiles obtained by van der Wel et al. (2012). For the background sky level of each cutout, we have modelled it in two different ways, namely to (1) set the sky as a free parameters and let GALFIT find the best-fit value and (2) fix the sky level to be the median pixel value derived from a 3σ clipping of the pixel values in the cutout image after masking out all H_{160} detected sources. It turns out that our results are insensitive to the method chosen so we decide to fix the sky level as the median pixel value of each cutout. We fit each target galaxy with a single 2-D Sérsic profile, from which we can directly obtain n and R_e ($= R_{e,maj} \times \sqrt{b/a}$), as well as $\Sigma_e = M_*/(2\pi R_e^2)$. With the best-fit Sérsic profile in hand, following the derivation of Graham & Driver (2005), we can get the fractional stellar mass within central 1 kpc through

$$\frac{M_{1\mathrm{kpc}}}{M_*} = \frac{\gamma(2n,\, x)}{\Gamma(2n)},\ x = b_n(\frac{1\mathrm{kpc}}{R_e})^{1/n} \qquad (3)$$

where γ/Γ is the ratio of incomplete gamma function divided by complete gamma function. When n>0.36, b_n is calculated using the approximate expression proposed by (Ciotti & Bertin 1999, their Equation 18, accurate to better than 10^{-4}), otherwise b_n is calculated by numerically solving $\Gamma(2n) = 2\gamma(2n, b_n)$. Finally, we can obtain the stellar mass surface density within central 1 kpc through

$$\Sigma_{1\mathrm{kpc}} = \frac{M_{1\mathrm{kpc}}}{\pi \cdot 1\mathrm{kpc}^2} = \frac{M_*}{\pi \cdot 1\mathrm{kpc}^2}\frac{\gamma(2n,\, x)}{\Gamma(2n)} \qquad (4)$$

Quantifying the uncertainty of these morphological parameters is non-trivial due to the covariance between parameters (e.g. Ji et al. 2020). In this work, we have conducted the covariance analysis by measuring the covariance between R_e and n for the entire AGN sample, aiming to estimate error bars of each aforementioned morphological parameter. To do so, we first run GALFIT to get the best-fit values of all free parameters and then use GALFIT to generate a number of models by changing n and R_e while fixing any other parameters to the best-fit values. We then calculate the χ^2 distribution of these new models to get the n-R_e covariance. Figure 5 shows covariances of the randomly-selected 9 AGNs with different H_{160} SNRs. Diverse shapes of the covariances are clearly seen even when sources have similar SNRs, demonstrating that the individual determination of n and R_e is non-trivial. For each AGN, we derive the 1σ uncertainty ranges of R_e and n using the covariance. We then plug all possible R_e-n combinations along the 1σ-χ^2 contour into Equation 3 to get the corresponding 1σ uncertainty of $\frac{M_{1\mathrm{kpc}}}{M_*}$. Figure 6 shows the

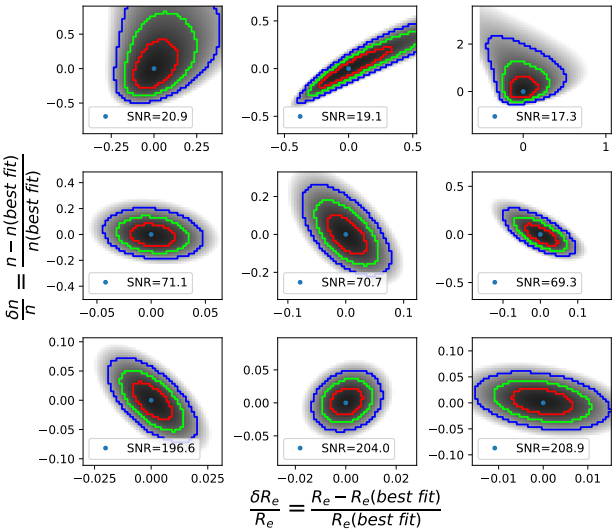

Figure 5. The R_e-n covariances of randomly selected 9 examples. The first, second and third rows show the cases with H_{160} SNR $\sim$ 20, 70 and 200 respectively. Red, green and blue lines show the corresponding 1σ, 2σ and 3σ confidence contours.

derived uncertainty as a function of H_{160} SNR. While the uncertainty overall decreases as SNR increasing, the uncertainty of different morphological parameters is different. For a detection with a descent SNR ($\geq$ 20), while R_e is reasonably well-constrained with a typical $\lesssim 10\%$ 1σ uncertainty, the uncertainty of n can be as large as $\approx 50\%$. Even for a SNR $\approx$ 100 detection, the uncertainty of n can still be $\approx 10\%$. Importantly, although n itself is usually not well-constrained, the measurement of $\frac{M_{1\mathrm{kpc}}}{M_*}$ (the combination of R_e and n) is about as good as R_e.

3.2.2. *Validity of the single Sérsic profile assumption*

We now test the validity of the single Sérsic profile assumption that we made so far for the morphological measurements. The non-stellar AGN radiation can "pollute" the stellar light distribution and hence introduce a systematic bias in the morphological measurements of host galaxies. To test for this systematic, we have re-done the morphological measurements assuming a different model, i.e. a 2D Sérsic profile plus a nuclear point source (Sérsic+PSF). Similarly as we did for the single 2D Sérsic profile fittings, we have also measured the covariances between R_e and n for the AGN hosts and derived the corresponding 1σ errors. In addition, Sérsic+PSF fittings have also been done among the non-AGNs in the GOODS-S, which we did in order

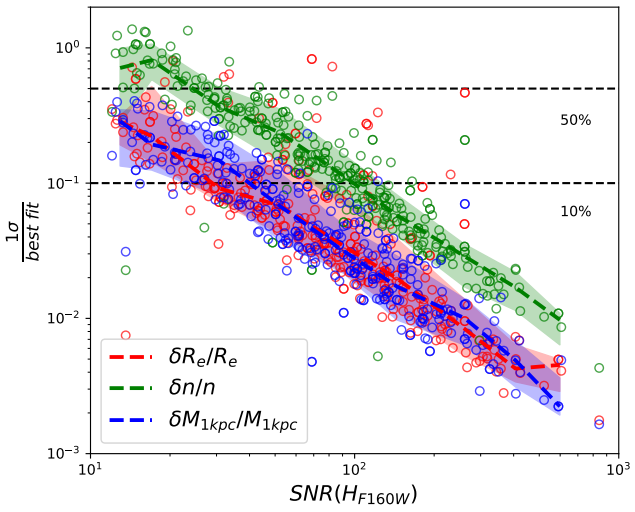

Figure 6. The uncertainty of R_e (red), n (green) and $\frac{M_{1kpc}}{M_*}$ (blue) as a function of H_{160} SNR. Y-axis shows the ratio of 1σ uncertainty divided by the best-fit value, where the 1σ range is from the covariance analysis (see Section 3.2 for details). Each circle shows the measurement of an AGN in our sample. The dashed lines show the median and the shadow regions show the 16th-84th percentile range. Also marked as the horizontal dashed lines are the 50% and 10% accuracy lines.

to compare with the AGNs. Figure 7 shows the comparisons of R_e, n and $\frac{M_{1kpc}}{M_*}$ between the assumed two different light profiles (Sérsic-only and Sérsic+PSF). We see clear correlations of R_e and $\frac{M_{1kpc}}{M_*}$ while a big scatter of Sérsic index n between the two measurements, suggesting a qualitatively *insensitive* dependence of R_e and $\frac{M_{1kpc}}{M_*}$, but a much more sensitive dependence of n on the assumed light distribution. This further supports what we have already found in Figure 6 that n is not as well-constrained as R_e and $\frac{M_{1kpc}}{M_*}$.

Compared with the Sérsic-only results, PSF+Sérsic leads to an increase of R_e and a decrease of $\frac{M_{1kpc}}{M_*}$, which is expected since adding a nuclear point source is equivalent to fit a single Sérsic profile to an image with some fraction of central light removed. In other words, if the nucleated component really has the non-stellar origin like an AGN, stellar morphology of the host galaxy should be more extended (larger R_e and smaller $\frac{M_{1kpc}}{M_*}$) than it is seen from the image. Owing to the limited image depth and spatial resolution at high redshift, however, it is hard to conclusively say if adding the central component to the fitting is physically necessary. For example, we notice that the fitting χ^2 generally improves after adding the nuclear point-like component. In particular, the reduced-χ^2 improves by 10% for the PSF+Sérsic model. But, we do not know if the improvement of χ^2 indicates the physical requirement of the central component, or simply because the PSF+Sérsic model has more free parameters than the Sérsic-only model and (of course) can fit the data "better". We can in principle compare the χ^2 change with the expected change that can be theoretically calculated if all the parameters are *independent* (which unfortunately is not the case, see Figure 5). Even if one can prove that the nucleated point-like source is a physically necessary component, it remains difficult to definitely disentangle its origin, which could be the non-stellar light from an AGN, or the stellar light from galaxy central structures like bulge, or both. It is worth mentioning here that, based on the PSF+Sérsic fitting results, we find a significant positive correlation, with a Pearson correlation test p-value of 7×10^{-5}, between AGN luminosity and F_{PSF}/F_{Sersic}, i.e. the flux ratio of the PSF component divided by the Sérsic component. While such correlation can be simply explained in terms of the AGN contamination being more severe to the rest optical stellar morphology as the AGN becomes more luminous, we do find evidence that the real cause(s) behind *cannot* merely be the AGN contamination. We defer detailed analysis and discussions of this issue to an upcoming paper.

Distributions of the relative changes of R_e, n and $\frac{M_{1kpc}}{M_*}$ are shown in the bottom panels of Figure 7, where relative changes are larger for the AGN hosts than normal galaxies. Interestingly, compared with IR AGNs, the relative changes also seem to be larger for X-ray AGNs, which is consistent with the scenario that X-ray AGNs are less (relative to IR AGNs) obscured such that the central AGN light "contanminates" the optical stellar morphology more for X-ray AGNs. The findings above seem to suggest that AGNs either require an extra nuclear non-stellar component for the morphological fitting, or to be preferentially embedded in galaxies that have developed a central compact structure, or both. Regardless of the actual physical reasons, which we will investigate in a future work, our findings suggest that the two component fitting for AGN hosts very likely is required and removing the nuclear light can reduce the correlation between AGN presence and galaxy compactness that has been found in previous works. Given the magnitudes of relative changes of R_e and $\frac{M_{1kpc}}{M_*}$, however, we have checked that this will not change our conclusions that AGN prevalence is fundamentally tied to mass more so than compactness (see Section 4.2.1 and 4.2.2). In the subsequent analysis, we will use the morphological parameters measured from the Sérsic-only fittings.

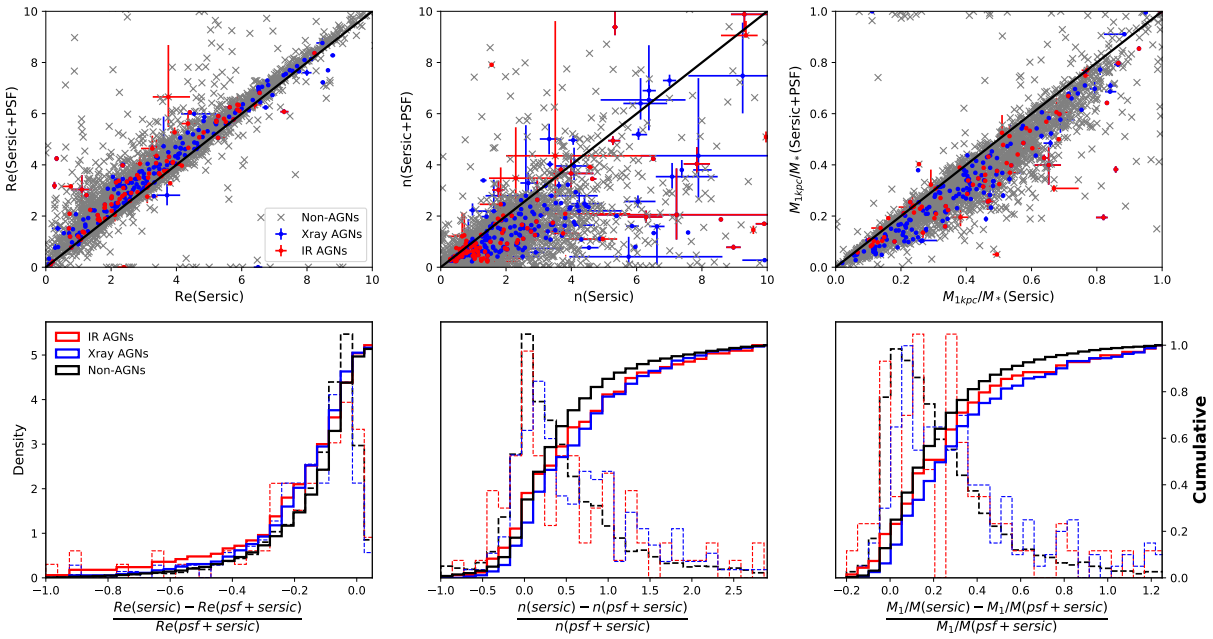

Figure 7. The comparisons of morphological parameters from the two different assumed light profiles, i.e. Sérsic-only and Sérsic+PSF models (see Section 3.2.2 for details). X-ray, IR AGNs and non-AGNs are color-coded with blue, red and grey respectively. The black solid line marks the one-to-one relation. The bottom panels show distributions and cumulative distributions of the relative changes of each individual parameter.

3.2.3. *Quantify galaxy compactness with* $\frac{M_{1kpc}}{M_*}$

We now detail our motivations and the advantages of using $\frac{M_{1kpc}}{M_*}$. This parameter measures the fractional stellar mass within the central 1 kpc and is a metric that quantifies the compactness of a galaxy. To check the effectiveness of this metric, in Figure 8, we compare $\frac{M_{1kpc}}{M_*}$ with other commonly-used morphological metrics, namely Petrosian radius R_p (Petrosian 1976), Gini, M_{20} (Lotz et al. 2004) and Σ_{1kpc}. We see that $\frac{M_{1kpc}}{M_*}$ does contain information on galaxy compactness in the sense that galaxies with large $\frac{M_{1kpc}}{M_*}$ statistically are also compact according to other metrics, i.e. large Gini, small M_{20}, small R_p and larger Σ_{1kpc}.

As we already discussed in Section 3.2.1, $\frac{M_{1kpc}}{M_*}$ can be measured with reasonably small uncertainty. Much more importantly, unlike the commonly-used compactness metrics like Σ_{1kpc} and Σ_e which are biased toward more massive galaxies (see details in the next paragraph), the dependence of $\frac{M_{1kpc}}{M_*}$ on M_* is much weaker, which can be explicitly seen from Equation (5). This can also be shown using the existing measurement of the $\text{Log}\Sigma_{1kpc}$-$\text{Log}M_*$ correlation. For example, in CANDELS/GOODS-S, for this correlation Barro et al. (2017) reported a strong but sub-linear relationship with slope of $\beta \approx 0.9$ and 0.7 for SFGs and QGs, respectively. The slopes do not change across the redshift range $0.5 < z < 3$. If we assume these slopes, we can then get the slope for the $\text{Log}\frac{M_{1kpc}}{M_*}$-$\text{Log}M_*$ correlation, which should be -0.1 for SFGs and -0.3 for QGs. In both cases, $\frac{M_{1kpc}}{M_*}$ have much weaker dependence on M_*. Using our sample, Figure 9 further demonstrates that the strong M_*-dependence of Σ_{1kpc} is largely eliminated when using $\frac{M_{1kpc}}{M_*}$, and only a slightly decreasing trend with $\frac{M_{1kpc}}{M_*}$ still persists for non-AGNs. This is from the low-mass ($\text{Log}M_* < 10$) galaxies in our sample, because the 1 kpc scale (compared with galaxy sizes [1]) probes a relatively larger area for a low-mass galaxy than for a high-mass galaxy, which naturally results in generally larger $\frac{M_{1kpc}}{M_*}$ for low-mass galaxies. The trend is much less obvious (it even disappears) for AGN hosts because AGNs are preferentially embedded in more massive galaxies (also see Section 4.2.2).

The criterion commonly used to select compact galaxies in literature are essentially a threshold cut on stellar mass surface density Σ, which can be formularized as

$$\text{Log}\,\Sigma > \alpha \text{Log}\,M_* + \beta \qquad (5)$$

[1] If we assume the van der Wel et al. (2014) mass-size relation for SFGs, the median R_e of a $10^{11} M_\odot$ galaxy is ≈ 4 kpc at z$\sim$2, while it is 2.6 (1.6) $\times$ smaller for a 10^9 (10^{10}) $M_\odot$ galaxy.

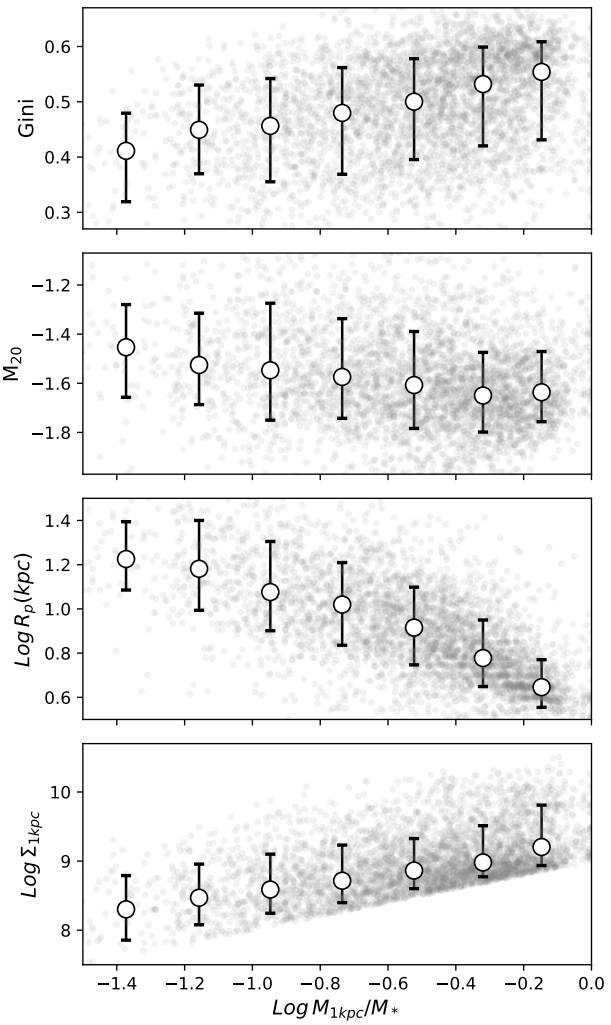

Figure 8. $\frac{M_{1kpc}}{M_*}$ vs Gini, M_{20}, R_p and Σ_{1kpc}. Individual galaxies are shown as grey dots. The circles with error bars show the median and 16th to 84th percentile range.

If we select compact galaxies using a fixed threshold of Σ, i.e. $\alpha = 0$, then Equation 5 becomes $\mathrm{Log}\Sigma > \beta$. Given that galaxies follow the well-defined size-mass relation with the form $\mathrm{LogR} \propto \eta \mathrm{LogM_*}$ (e.g. van der Wel et al. 2014), the selection criterion then becomes $(1-2\eta)\mathrm{LogM_*} >$ constant. We can now explicitly see that more massive galaxies are more likely to be selected as compact unless $\eta = 0.5$, which however is not the case (e.g. use the R_e-Σ_e relation of Barro et al. 2017, η is ≈ 0.2 for SFGs and ≈ 0.8 for QGs). To reduce this M_* bias, one can then use a M_*-dependent threshold cut on Σ, i.e. $\alpha \neq 0$ (e.g. Barro et al. 2013; Kocevski et al. 2017; Wang et al. 2018). Now, Equation 5 becomes to $(1-2\eta)\mathrm{LogM_*} > \alpha \mathrm{LogM_*} +$ constant. The bias in

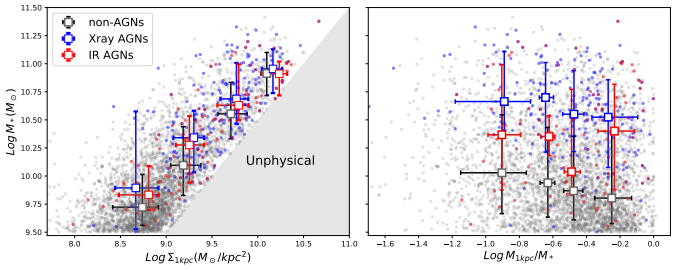

Figure 9. Scatter plots of M_* vs. Σ_{1kpc} (left) and M_* vs. $\frac{M_{1kpc}}{M_*}$ (right). It is obvious that the dependence on M_* is much weaker for $\frac{M_{1kpc}}{M_*}$ than for Σ_{1kpc}.

principle can be fully removed by choosing $\alpha = 1-2\eta$. However, the size-mass relation depends on galaxy properties. For example, observations have shown that SFGs and QGs follow different relations (e.g. Newman et al. 2012; Law et al. 2012; Barro et al. 2017). This means that, even with the M_*-dependent threshold cut on Σ, the bias still cannot be fully removed. The bias remains in at least one galaxy population (SFGs or QGs). This selection bias becomes particularly important for data interpretation when trying to identify the driven factor (e.g. mass vs morphology) of some observed correlations. For example, as will be discussed later in Section 4.2.2, we find that the prevalence of AGNs positively correlates with Σ_{1kpc}. However, since Σ_{1kpc} positively correlates with M_* and the prevalence of AGNs also increases with M_*, we do not know if the observed AGN prevalence-Σ_{1kpc} correlation is due to M_*, or actually infers the causation between the prevalence of AGNs and galaxy compactness.

To this end, we highlight the advantage of using $\frac{M_{1kpc}}{M_*}$. Because of its weak dependence on M_*, any relation observed with $\frac{M_{1kpc}}{M_*}$ should be primarily caused by galaxy morphology.

4. RESULTS

In this Section, we aim to investigate the observational evidence of the effects of AGN presences on host galaxies. In the following, we will first compare the star formation properties of AGNs with non-AGNs (Section 4.1.1 and Section 4.1.2), and then investigate if the AGN prevalence changes with the star formation properties of their hosts (Section 4.1.3). We will then compare the morphological properties of AGNs and non-AGNs (Section 4.2.1), and then investigate if the AGN prevalence changes with the morphological properties of their hosts (Section 4.2.2).

4.1. *Star formation properties*

4.1.1. *Distributions of AGNs on the star forming main sequence*

In Figure 10, we compare the distributions of AGNs with normal SFGs on the star-forming main sequence (SFMS), i.e. specific star formation rate (sSFR) vs M_*. The medians and 1σ (16th–84th) ranges for individual populations are derived in two ways. A common way is to compute median and inter-quartile sSFR in arbitrarily defined M_* bins, which are shown as squares with error bars in the main panel of the Figure. The other way of calculating the percentiles is to use the non-parametric quantile regression, in which case no arbitrarily defined bins are required. Here, we adopt the COnstrained B-Splines (COBS, see Ng & Maechler 2007, 2020 for details) package in R to carry out the quantile regressions, where the total number of knots required for the regression B-spline method is determined using the Akaike-type information criterion. The results from COBS are inserted to the bottom left of the main panel. Regardless of the way to calculate the median relation, we find that, while the median sSFRs of X-ray AGNs are indistinguishable to normal SFGs, enhanced sSFR is observed in IR AGN hosting galaxies.

Two tests have been done in order to check the robustness of the conclusions above. First, the SFR comparisons in Section 3.1 have shown that our SED fittings can on average over-estimate SFRs for AGN hosting galaxies by ≈ 0.1 dex due to the ignorance of AGN components. However, the magnitude of this systematics is small compared with the scatter of sSFR distribution of X-ray AGNs and, it is also smaller than the strength of sSFR enhancement (~ 0.4 dex) as seen for the whole sample of IR AGNs. We therefore do not expect such over-estimation can significantly affect our sSFR comparisons. Second, different M_* and redshift distributions of AGNs and non-AGNs can potentially affect our sSFR comparisons because of the evolution of the SFMS (e.g. Whitaker et al. 2014; Lee et al. 2018). We test this by building the M_*-z-matched subsample of non-AGN SFGs, whose sSFR distribution is then used to compare with that of AGNs. We do this in three M_* bins, and for X-ray and IR AGNs *separately,* since their M_* and redshift distributions are also different from each other. For each AGN, we select the two non-AGN SFGs which are the closest to the AGN in the M_*-z space to build the M_*-z-matched subsample. We have checked that our conclusions below do not depend on how the M_*-z-matched subsample is built. For instance, we have tried building the subsample by randomly selecting two/three non-AGN SFGs whose redshifts are within $\delta z < 0.2$ and M_* are within $\delta LogM < 0.3$, and the results remain unchanged.

Figure 11 shows the detailed comparisons of sSFR distributions for AGNs and non-AGN SFGs. The median sSFR for X-ray AGNs is similar to that of the M_*-z-matched, non-AGN SFGs, except in the smallest M_* bin (i.e. $9.5< \mathrm{Log}M_* <10$), where the X-ray AGN sample suffers from small number statistics. In spite of the similar medians, the two sample Kolmogorov–Smirnov tests indicate that we can reject the null hypothesis that the two (matched non-AGN SFGs and X-ray AGNs) sSFR distributions are identical with a $91.6 \sim 99.7\%$ (i.e. 1.7-3σ, depending on the M_* bins, see the Figure for details) confidence level. Compared with the M_*-z matched non-AGN SFGs, an enhanced sSFR in IR AGNs is still observed, although the magnitude shrinks from ≈ 0.4 to 0.3 dex. A similar enhancement strength is seen in all three M_* bins. The two sample Kolmogorov–Smirnov tests indicate that we can reject the null hypothesis that the two (matched non-AGN SFGs and IR AGNs) sSFR distributions are identical with a $93.5 - 99.6\%$ (i.e. 1.8-3σ) confidence level, which, as can be seen in the Figure, is likely driven by the shift toward high sSFR for IR AGNs. To this end, we conclude that, rather than measurement uncertainty or different M_* and z distributions between AGNs and non-AGNs, our results do suggest the median sSFR of (1) IR AGNs is enhanced and (2) that of X-ray AGNs is indistinguishable relative to normal SFGs. In addition, our Kolmogorov–Smirnov tests indicate the entire sSFR distribution for AGNs, either X-ray or IR selected, are different from normal SFGs with a $\approx 2 - 3\sigma$ confidence level.

For IR AGNs, the enhancement of star formation has also been reported by other works (e.g. Cowley et al. 2016; Ellison et al. 2016; Azadi et al. 2017). The widely-accepted interpretation of it is galaxy merger, a violent process that naturally can both ignite starbursts and fuel luminous AGNs (Sanders et al. 1988, also see Figure 6 in Alexander & Hickox 2012 for a schematic view). The observational supports on this scenario primarily come from the morphological studies of host galaxies of IR AGNs. Satyapal et al. (2014) studied a sample of WISE-selected AGNs in SDSS, from which they showed the probability to find IR AGNs in post-merger systems is $\approx 10 - 20$ times higher than the control sample. Similar conclusions have also been made by using different MIR selections and at higher redshifts. For instance, Donley et al. (2018) adopted IRAC-color selection criteria (the same as used in this work) to study IR AGN populations at $z \lesssim 3$ in the CANDELS/COSMOS, from which they concluded that IR AGNs are significantly more likely to be found in interacting/merging

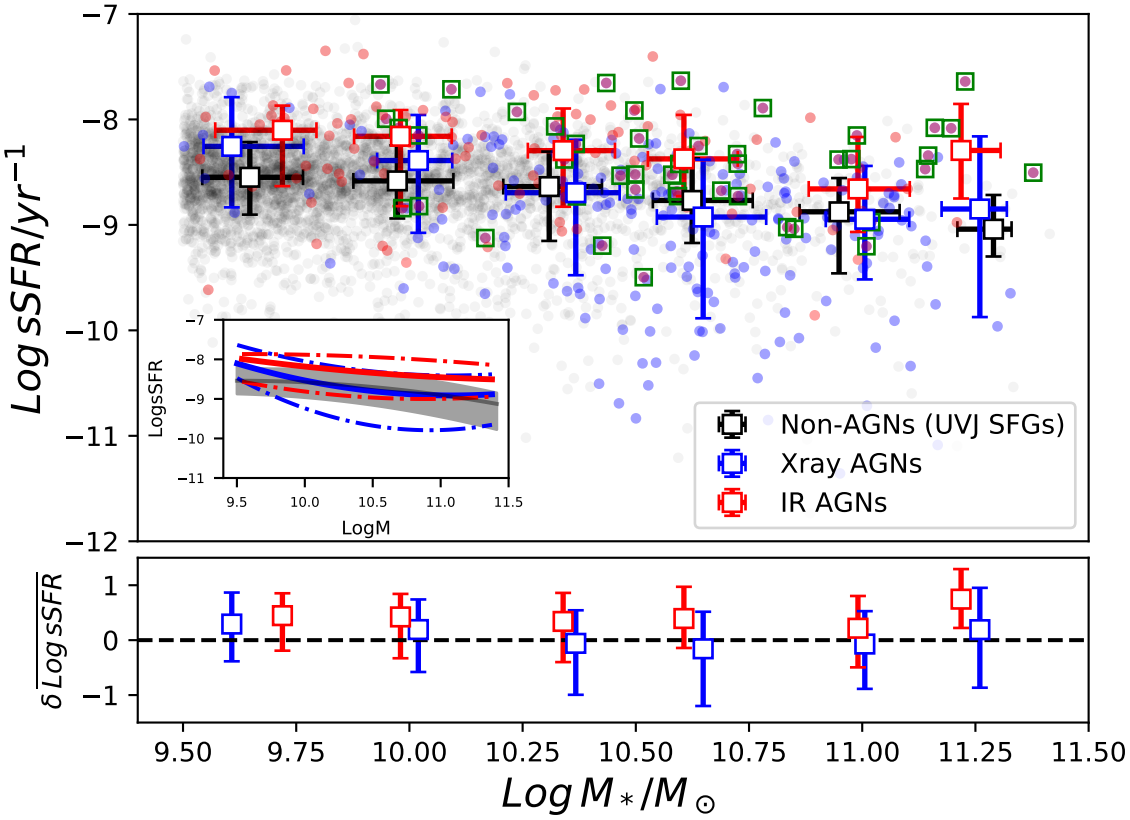

Figure 10. AGNs and normal SFGs on the sSFR-M$_*$ diagram. X-ray, IR AGNs and non-AGNs are shown as blue, red and black dots respectively. The corresponding color-coded circles with error bars show the median and 16th–84th percentiles of sSFR in each M$_*$ bin. AGNs that are identified as both X-ray and IR AGNs are labelled with green squares. The inset on the bottom left of the main panel shows the medians and 16th–84th ranges for individual populations derived by COBS in R using the Constrained B-splines interpolations. The bottom panel shows differences of the mean sSFR between AGNs and non-AGNs in each M$_*$ bin.

systems compared with Seyfert-like AGNs. These, in turn, can also explain why this IR selected AGN population is missed in X-ray since obscuration correlates with merger stage and SMBHs can grow during highly obscured stages of galaxy mergers. If the IR selection is more efficient in picking up the AGNs triggered by galaxy mergers/interactions, then we would expect to see the host galaxies of IR AGN to have enhanced star formation activities, as being the consequence of galaxy mergers/interactions. Based on the sSFR comparison itself, nothing can be said on whether on-going AGN activities have any casual connection with galaxy-wide star formation or not, as the effects (if any) can be easily "buried" beneath the effects produced by mergers/interactions.

For X-ray AGNs, while their median sSFR is indistinguishable from normal SFGs, the sSFR distribution of the X-ray AGNs hosted by massive galaxies (LogM$_* \gtrsim$ 10.3) is skew to low sSFRs. Moreover, among the massive X-ray AGN hosts, those with high sSFRs often are also identified in IR. If we look at the AGNs which are merely identified by X-ray, skewness to low sSFRs becomes even more clear. These are consistent with the conclusions of Mullaney et al. (2015), where they found that the mass and redshift-normalized SFR distributions of their X-ray AGNs are broader and peaked at lower value than normal main sequence SFGs, despite that mean SFRs for the two populations are similar. The interpretation of the results above is non-trivial owing to different timescales involved. While AGN is instantaneous, SFR is not. One would be able to measure

instantaneous SFR if a correct SFH were known. As a result, no causal link can be indicated merely based on the SFR comparisons between AGNs and normal SFGs unless AGNs have been "on" for the same timescale as SFRs are being traced. Even so, the interpretation of the similar median sSFRs between AGNs and normal SFGs is not unique. If a time lag (longer than the timescale of the current star formation episode) is required to enable AGN feedback effects being observable, not too much can be said by looking at on-going AGNs. Alternatively, although the fine-tuning of AGN feedback is required, the observed similar median sSFRs can also be produced by the equally positive and negative feedback of X-ray AGNs. The latter one, however, seems to be disfavored by the observed independency (although error bars are large) between AGN luminosities and star formation activities (Section 4.1.2).

4.1.2. *AGN luminosity vs. Starburstiness*

Phenomenologically speaking, if AGN activities do *instantaneously* affect galaxy-wide star formation, a correlation between AGN luminosities and their hosts' star formation properties is expected. We therefore study the relation between AGN bolometric luminosities (L_{bol}) and starburstiness (R_{SB}), which is defined as the SFMS-normalised sSFR,

$$R_{SB} = \frac{sSFR}{sSFR(z, M_*)} \quad (6)$$

where sSFR(z,M_*) is the sSFR for a galaxy on the SFMS with M_* at z. We adopt the SFMS measured by Lee et al. (2018), as the relation was measured upon the same galaxy sample using the same SED fitting algorithm.

The details of L_{bol} measurements can be found in Ji et al. 2021 in prep. (to be submitted) and we only briefly outline the key steps here. For X-ray AGNs, we first take intrinsic X-ray 0.5-7 keV luminosities from Xue et al. (2016) and Luo et al. (2017), which were measured by correcting the observed X-ray flux with the obscuration empirically calibrated by X-ray band ratios. We assume an AGN spectral photon index $\Gamma = 1.8$ and convert the intrinsic 0.5-7 keV to intrinsic 2-10 keV luminosities, which are finally converted to L_{bol} using the 2-10 keV bolometric correction from Hopkins et al. (2007). For IR AGNs, we first obtain the AGN monochromatic luminosities at 15μm using the best-fit SED decomposition by SED3FIT and convert them to L_{bol} using the 15μm bolometric correction of Hopkins et al. (2007). The 15μm-derived L_{bol} is consistent with the direct L_{bol} output from SED3FIT (the difference between the two is -0.15±0.2 dex). We have checked that our conclusions are not sensitive to the choice of MIR derived L_{bol}, i.e. 15μm-derived one and direct output from SED3FIT.

To check the robustness of the measurements, we first checked that our measurements of the ratio of AGN 2-10 keV luminosity divided by AGN IR luminosity are in good agreement with Kirkpatrick et al. (2017). We have also further compared the MIR-derived with X-ray-derived L_{bol} for X-ray AGNs and found that the two L_{bol} are consistent with each other when $L_{bol} \gtrsim 10^{43.5}\, erg/s$ (see Figure 12 and a detailed discussion in Ji et al. 2021 in prep.), although the scatter between the two measurements is large, with a typical ±0.5 dex which will hopefully be much improved with the coming MIR capability of JWST and future more sensitive X-ray telescopes. Since only a small fraction of the AGNs are fainter, we have checked that including/excluding those faint AGNs cannot affect our conclusions.

In Figure 13, R_{SB} is plotted against L_{bol}. IR AGNs in our sample are in general brighter than X-ray AGNs by ≈ 0.5 dex, indicating that the IRAC-color selection adopted by us is less sensitive, hence detects only most powerful AGNs. The $L_{bol} - R_{SB}$ correlation is neither seen for X-ray AGNs nor seen for IR AGNs, which seemingly suggests that *instantaneous* AGN activities do not affect galaxy-wide star formation. We point out, however, that the measurement uncertainty of the relation, particularly along the L_{bol} axis, is large which may potentially wash out an existing trend. Moreover, stochastic AGN variability can easily weaken the correlations between the observed AGN activities and the star formation properties of AGN hosts (Hickox et al. 2014).

While the overall trend between L_{bol} and R_{SB} is unclear, we do notice that the galaxies with the most intense star formation activities (i.e. the highest R_{SB}) seem to also have the most powerful AGNs. In addition, we also see very tentative evidence that, for X-ray AGNs, the median L_{bol} is smaller at the low-end of R_{SB} although the scatter is very large. Like we did in Section 4.1.1, we also use the constrained B-splines regressions (i.e. COBS) to get the L_{bol}–R_{SB} quantile curves (top-left inset of Figure 13), according to which we reach the similar conclusions. These findings are consistent with the X-ray stacking results obtained by Rodighiero et al. (2015), where they found an enhancement (deficit) of X-ray luminosity in their stacked starburst (green valley) galaxies. Possible interpretations of the enhanced X-ray flux in starburst systems are (1) starbursts are more X-ray active just as they are more star forming (Rodighiero et al. 2015 reported a factor of 2 larger BH accretion rate per star formation rate (BHAR/SFR) for starbursts than galaxies on the SFMS) and (2) the increasing fraction of AGNs driven by mergers as L_{bol} in-

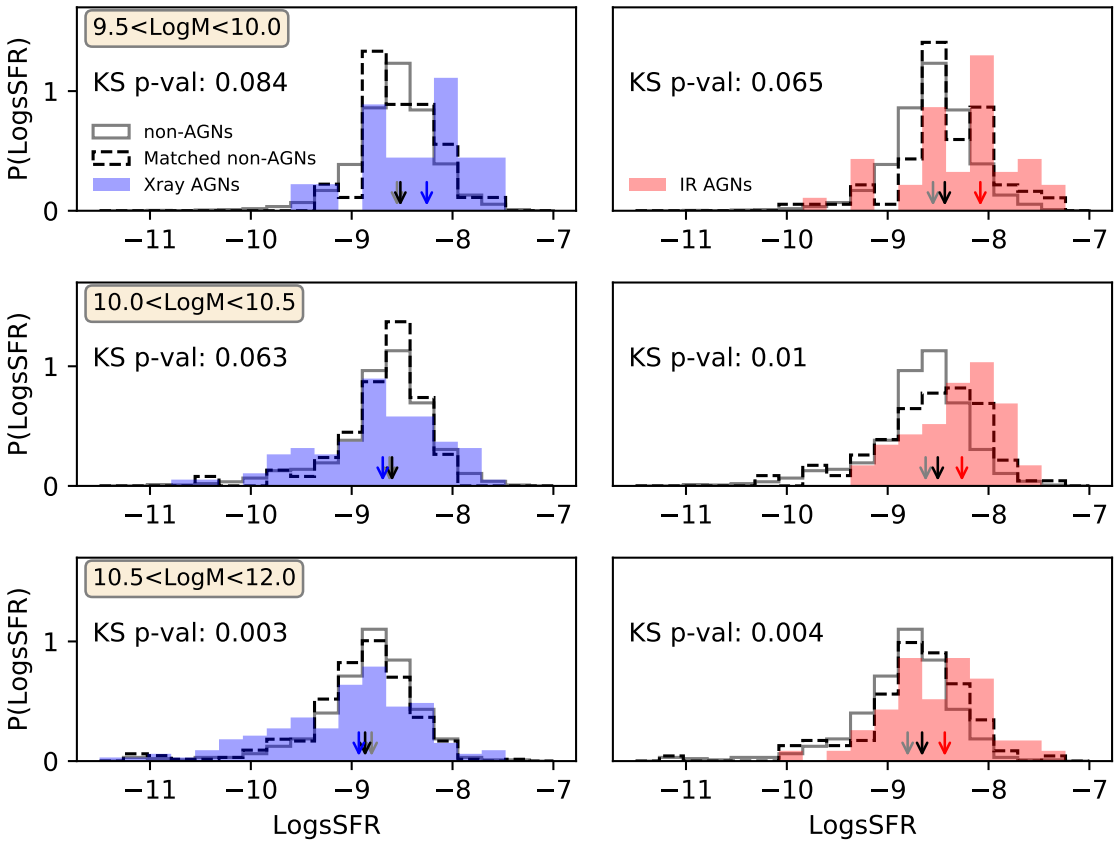

Figure 11. Comparisons of distributions of sSFR in the three M_* bins, namely 9.5< LogM$_*$ <10 (1st row), 10< LogM$_*$ <10.5 (2nd row) and 10.5< LogM$_*$ <12 (3rd row). The comparisons are between AGNs, where X-ray AGNs are shown in blue in the left panels and IR AGNs are shown in red in the right panels, and non-AGN SFGs, where the entire non-AGN SFGs are shown in grey and M$_*$-z-matched non-AGN SFGs are shown in black. Down arrows in each panel show the medians of individual distributions. Also labelled in each panel is the p-value of the two sample Kolmogorov–Smirnov test for the null hypothesis that the sSFR distribution of AGN (either X-ray or IR selected) hosting galaxies is identical to that of M$_*$-z-matched non-AGN SFGs.

creasing, which has been observationally demonstrated by Treister et al. (2012).

Finally, we look into the relation of R_{SB} with AGN bolometric luminosity per stellar mass (L_{bol}/M_*). Similar as what have been found for L_{bol}, Figure 14 shows that (1) L_{bol}/M_* is larger for our IR-selected AGNs and (2) no clear correlation is seen between L_{bol}/M_* and R_{SB}. Unlike that L_{bol} measures the total radiative energy released from a SMBH, L_{bol}/M_* measures its accretion efficiency [2]. The larger L_{bol}/M_* suggests a higher accretion efficiency for IR AGNs than X-ray AGNs, which possibly indicates different fueling mechanisms of SMBHs. While X-ray AGNs are more likely powered by the stochastic fueling processes like secular evolution of galaxies themselves or galactic disk instabilities, IR AGNs are likely triggered by the violent events like galaxy mergers, which are consistent with the findings of morphological studies of AGN hosts (e.g. Kartaltepe et al. 2010; Cisternas et al. 2011; Kocevski et al. 2012; Villforth et al. 2014; Ellison et al. 2016; Donley et al. 2018). Consistent results have also been found recently by Delvecchio et al. (2020), where they empirically modelled AGN luminosity functions for galaxies on and above the SFMS. They found that higher *Eddington Ratios* are required to reproduce the luminosity function for starburst galaxies.

[2] Note that L_{bol}/M_* can be easily converted to the *Eddington Ratio* by assuming a M$_{BH}$-M$_*$ relation

4.1.3. *AGN prevalence vs. star formation properties*

We now investigate the dependence of the AGN prevalence on star formation properties of host galaxies.

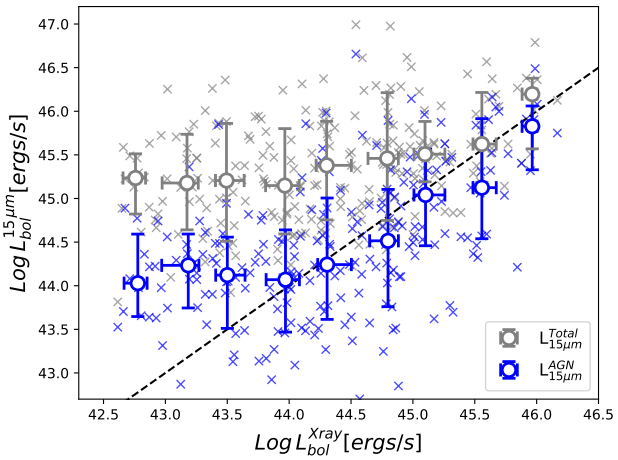

Figure 12. The comparison between X-ray- and 15 μm-derived L_{bol} for X-ray AGNs. Two values of $L_{15\,\mu m}$ from SED3FIT are used to calculate $L_{bol}(15\mu m)$. One is the total (AGN+stellar) $L_{15\,\mu m}^{Total}$ (grey x), the other is the best-fit AGN *only* $L_{15\,\mu m}^{AGN}$ (blue x). The circles with error bars show the medians and 16th-84th percentile ranges. The black dashed line marks the one-to-one relation. This comparison shows the essential role that SED decomposition plays in deriving correct L_{bol}.

The prevalence of AGNs is quantified by AGN fraction (q_{AGN}) which is defined as the ratio of the number of AGNs (N_{AGN}) divided by the total number of galaxies ($N = N_{AGN}+N_{nAGN}$), i.e. $q_{AGN} = N_{AGN}/N$. The three panels of Figure 15 show the changes of q_{AGN} with SFR, sSFR and R_{SB} respectively. Recall that both sSFR and R_{SB} are essentially normalized SFR, with the former being normalized by M_* and the latter being normalized by both M_* and z.

We start with the prevalence of X-ray AGN. First, regardless of the adopted metric of star formation intensity (SFR, sSFR or R_{SB}), q_{AGN} is high in galaxies with intense star formation activities. Second, for galaxies with normal/suppressed star formation rates LogSFR$\leq$1.5, q_{AGN} stays approximately flat with SFR. Because both SFR and q_{AGN} increase with M_* (the q_{AGN}-M_* relation will be studied in Section 4.2.2), normalizing SFR with M_* (i.e. sSFR) can effectively mitigate the M_* dependence to allow a more direct view on the link between q_{AGN} and star formation activities. Compared with galaxies with moderate sSFR (~ 1 Gyr^{-1}), a higher incidence of X-ray AGNs is observed in galaxies with suppressed sSFR (also have green colors, which will be shown in Section 4.2.1). A similar trend is also seen when using R_{SB} which mitigates not only the M_* but also redshift dependence by normalizing each galaxy with the SFMS. The findings above are consistent with what have been reported by Aird et al. (2019) (see their Figure 10 and 11 in particular), where they showed that the X-ray AGN prevalence is larger both for galaxies with suppressed star formation and for starbust galaxies, although it should be pointed out that, apart from galaxies with X-ray detections, they adopted a Bayesian methodology to also include the X-ray information for galaxies lacking direct flux detection into their analysis while we do not follow such an approach here.

Unlike X-ray AGN prevalence, q_{AGN} of IR AGNs generally increases with SFR, sSFR and R_{SB}. The increasing q_{AGN} towards galaxies with intense star formation is consistent with the picture of merger-driven scenario. Compared with X-ray AGNs, the unseen over-abundant IR AGNs hosting by galaxies with suppressed star formation show the differences between the two AGN populations, highlights the importance of the AGN selection effect (e.g. X-ray vs IR) in altering the distribution of host galaxy properties and as a result in building up a comprehensive picture of AGN effects on host galaxies.

Finally, as we already discussed in Section 4.1.2, because the sensitivities of the two AGN selection methods are different, namely that the IR selection is less sensitive at fixed bolometric luminosity (Figure 13), the L_{bol} difference, in principle, can lead to the distinct q_{AGN} trends seen between X-ray and IR AGNs, if there is a strong dependence of star formation properties with AGN luminosity, which however is not seen (Section 4.1.2) despite of the still large uncertainty in the L_{bol} measurements. Nevertheless, we do test this possibility by setting a cut in L_{bol}, i.e. $10^{44}\,erg/s \leq L_{bol} \leq 10^{45.5}\,erg/s$, on both AGN populations. The cut at the low end of the L_{bol} distribution aims to exclude the faint AGNs that currently are not picked up by our IR selection. The high-end cut, on the other side, aims to exclude the brightest and highly obscured AGNs missed by the X-ray selection. As Figure 13 shows, both selection methods are similarly sensitive with the adopted L_{bol} range. As the bottom panels of Figure 15 show, our conclusions do not change after doing the L_{bol} cut.

4.2. *Morphological properties*

4.2.1. *Distributions of AGNs on color-morphology diagrams*

In this Section, we study how AGNs and non-AGNs distribute in the color-morphology parameter space. In particular, we study their distributions in the diagrams of dust-corrected rest-frame color $(U - V)_{corr}$ vs. Σ_e, Σ_{1kpc} and $\frac{M_{1kpc}}{M_*}$ respectively. The reasons of using $(U - V)_{corr}$, rather than $(V - J)_{corr}$, are that $(U - V)_{corr}$

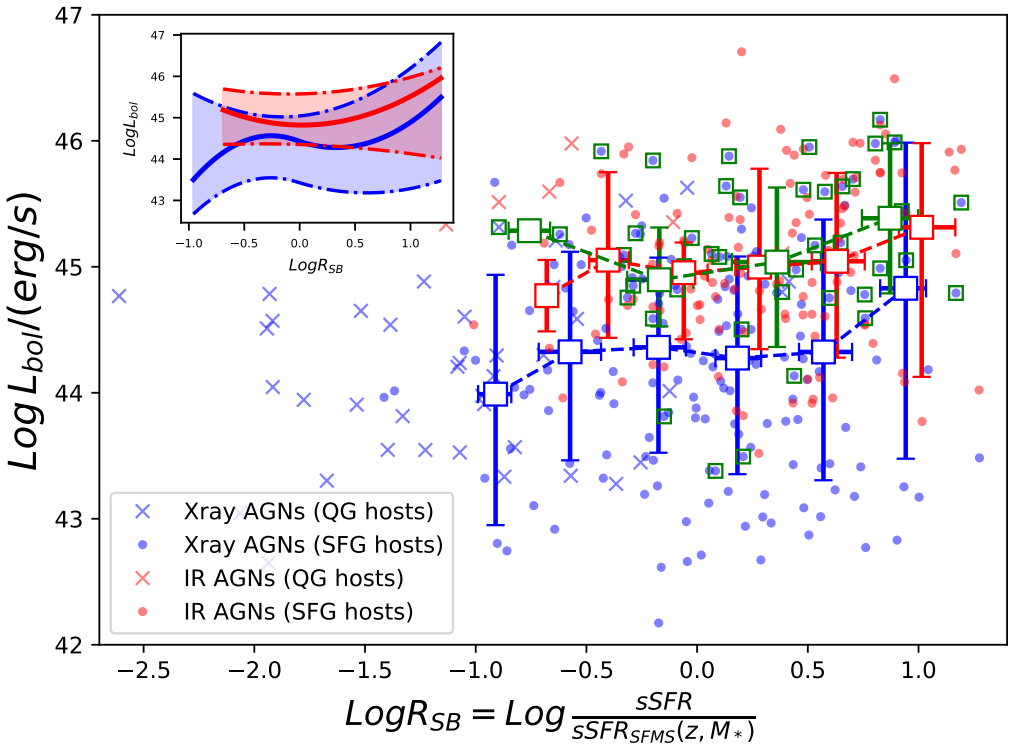

Figure 13. The R_{SB}-L_{bol} scatter plot of X-ray AGNs (blue), IR AGNs (red) and AGNs that are identified as both X-ray and IR AGNs (green). AGNs hosted by QGs are shown as 'X's. AGNs hosted by SFGs are shown as dots, with the mean and 16th-84th percentiles over-plotted as circles with error bars. The inset on the top left shows the medians and 16th–84th ranges for SFG hosting X-ray AGNs and IR AGNs derived by COBS in R using the Constrained B-splines interpolations.

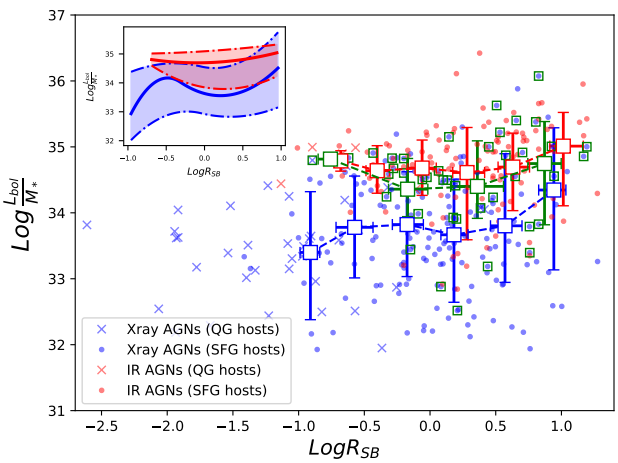

Figure 14. Similar as Figure 13, but y-axis is changed to L_{bol}/M_*.

(1) better probes star formation properties and (2) is less sensitive to the assumption of dust attenuation (see Figure 28). We notice that, after doing the dust correction, $(U - V)_{corr}$ itself can effectively separate SFGs and QGs (see Figure 16). The separation boundary is $(U - V)_{corr} \approx 1.1$ mag, fully consistent with Kocevski et al. (2017).

As Figure 16 shows, compared with non-AGNs, X-ray AGN hosts are over-abundantly seen to be hosted by galaxies with green $(U - V)_{corr}$ colors, which is consistent with Section 4.1.3 where the relations between q_{AGN} and star formation properties were investigated. Consistent conclusions also have been obtained by many other studies on X-ray AGNs, both in the local Universe (e.g. Martin et al. 2007; Salim et al. 2007; Schawinski et al. 2010) and at high redshifts (e.g. Nandra et al. 2007; Coil et al. 2009). With regard to morphological properties, compared with non-AGNs, X-ray AGNs share the similar locus of parameter space with QGs, which also have larger stellar mass surface density (Σ_e and Σ_{1kpc}) than SFGs. This fully aligns with the finding of Kocevski et al. (2017), where they reported a large fraction of compact SFGs hosting X-ray AGNs at $z \sim 2$.

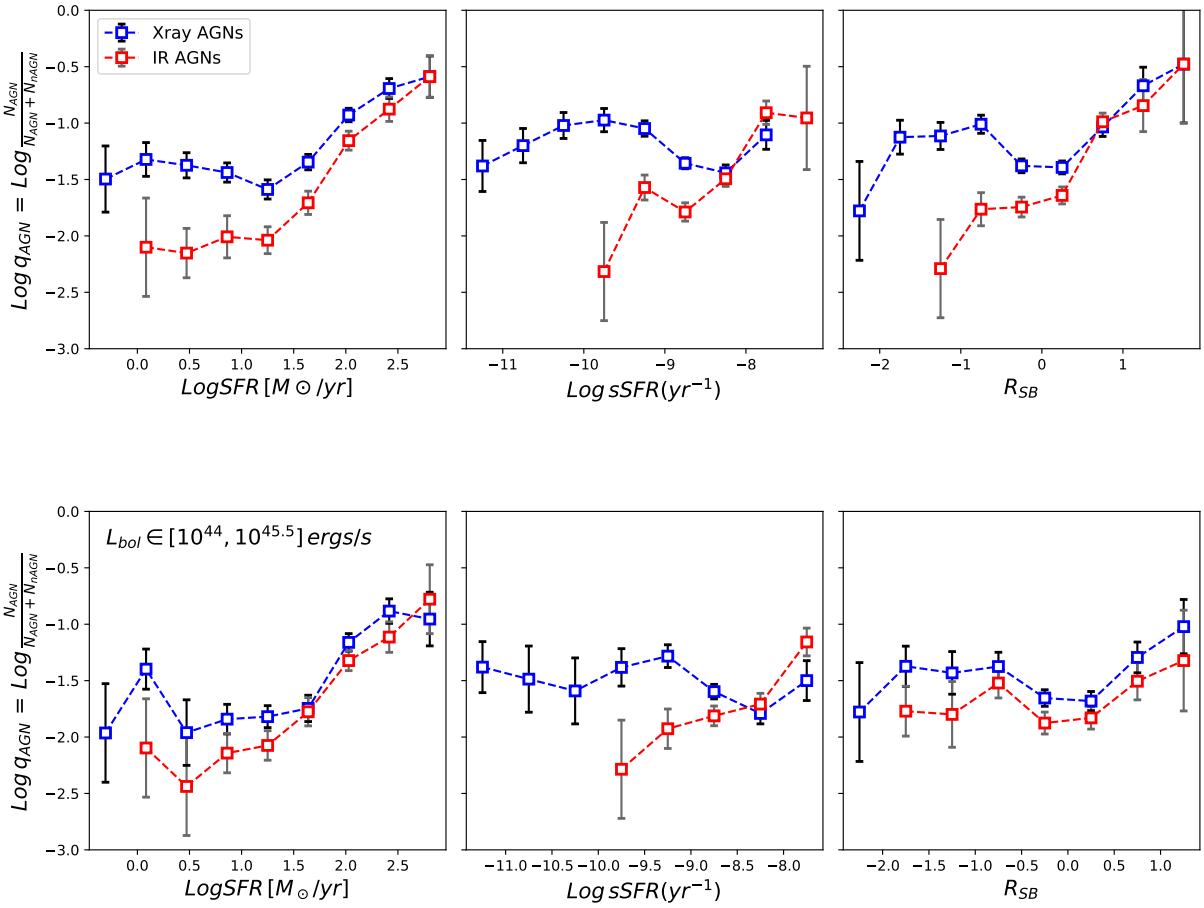

Figure 15. Upper: AGN prevalence vs. star formation properties. From left to right: the dependence of q_{AGN} on SFR, sSFR and R_{SB}. We refer readers to Figure 19 for the relation of AGN prevalence with M_*. **Bottom:** Similar to the upper panels, but a L_{bol} range cut ($10^{44} - 10^{45.5}$ erg/s) is posted on both AGN populations.

Figure 16 also clearly shows that IR AGNs distribute differently in the color-morphology space when compared with X-ray AGNs. Specifically, unlike X-ray AGN hosts peaked in the region with green colors, IR AGNs are bluer and have similar (but slightly redder) colors as normal SFGs. Meanwhile, while IR AGNs seem to have larger surface stellar mass density than SFGs, they are not as compact as X-ray AGNs, immediately showing the importance of AGN selection on the distributions of physical properties of AGN hosting galaxies.

Because both Σ_e and Σ_{1kpc} strongly and positively correlate with M_* (see Section 3.2.3), the observed larger Σ_e and Σ_{1kpc} of AGN hosts (both X-ray and IR) than SFGs can possibly be explained by the fact that AGN hosts are systematically more massive than non-AGNs (Section 4.2.2), rather than the intrinsic relation between galaxy compactness and AGN activities. To check this, in the right-most panel of Figure 16, $(U-V)_{corr}$ is plotted against $\frac{M_{1kpc}}{M_*}$, our compactness metric that only weakly depends on M_* (Section 3.2.3). Unlike using Σ_e and Σ_{1kpc}, the $\frac{M_{1kpc}}{M_*}$ distribution of AGNs is very similar to that of SFGs, suggesting *no* clear link between galaxy compactness and AGN activities. In addition, served as an alternative test, we have compared the Σ_e, Σ_{1kpc} and $\frac{M_{1kpc}}{M_*}$ distributions of AGNs with a sub-sample of M_*-matched non-AGNs (the upper panels of Figure 17). Similarly to what we did in Section 3.1, for each AGN, we selected the closest two non-AGNs in the M_*-z space. We have checked, by choosing the closest three/four non-AGNs, that our results do not change. After doing the M_*-z matching, the distributions of both Σ_e and Σ_{1kpc} of non-AGNs move toward larger values, making the tendency of AGNs being more compact *less obvious*. Also noticed in the Figure is that the $\frac{M_{1kpc}}{M_*}$ distribution does not significantly change after matching M_*, again showing the only weak M_*-dependence nature of $\frac{M_{1kpc}}{M_*}$ that has already been discussed in details in Section 3.2.3.

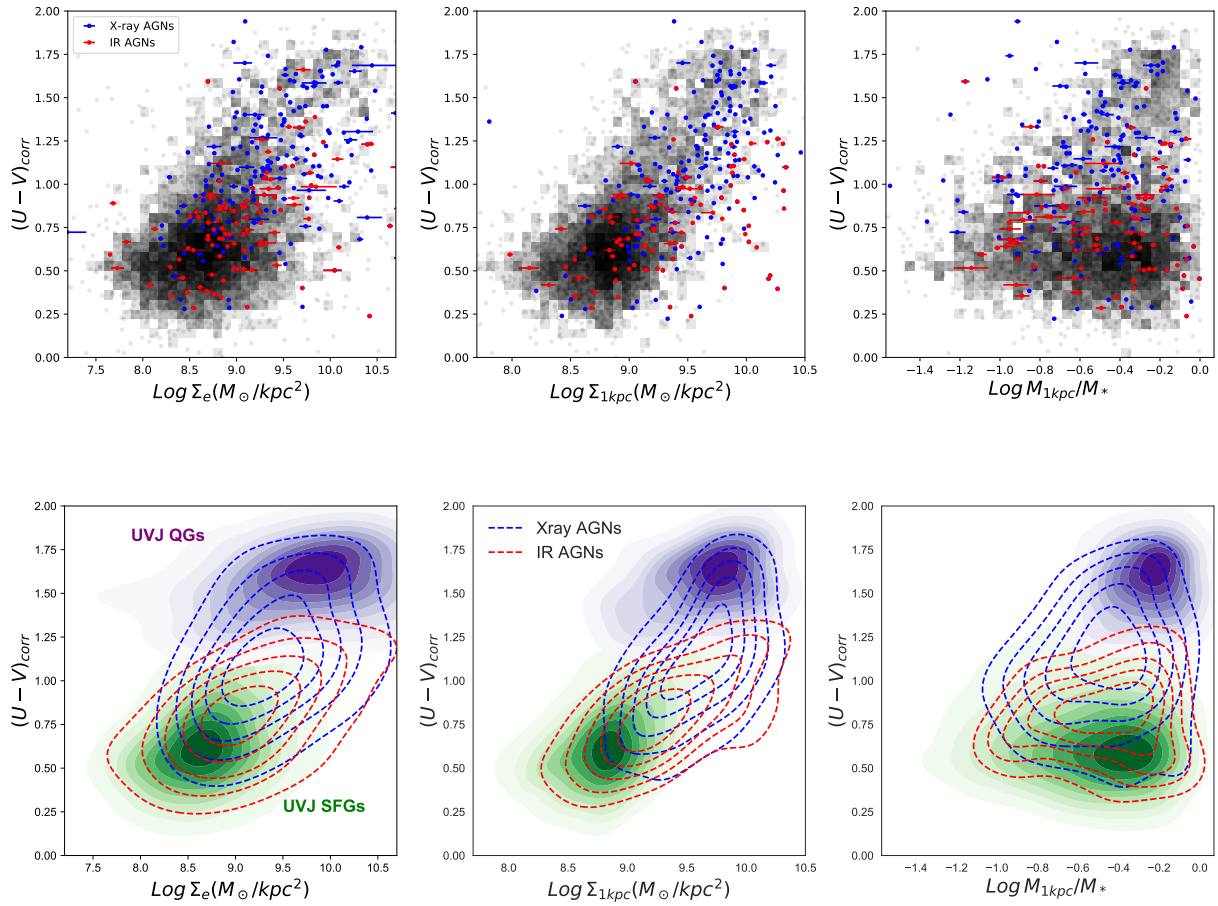

Figure 16. Dust-corrected rest-frame color $(U-V)_{corr}$ vs. morphological properties. **Upper:** Scatter plots for X-ray AGNs (blue dots), IR AGNs (red dots) and non-AGNs (black dots). From left to right, each panel shows $(U-V)_{corr}$ vs. Σ_e, $\Sigma_{1\rm kpc}$ and $\frac{M_{1\rm kpc}}{M_*}$ respectively. The 2-D histograms of non-AGNs are over-plotted in grey scales. **Bottom:** Number density distributions for AGNs and non-AGNs. Non-AGNs are further divided into star-forming (green) and quiescent (purple) galaxies according to the UVJ color-color diagram. The number density distributions are estimated using the Gaussian kernel.

Not only M_*, because of the different sensitivities of the two AGN selection methods, the L_{bol} difference could also result in the distinct color-morphology distributions seen between X-ray and IR AGNs, if L_{bol} somehow plays a crucial role in determining host galaxies' colors and morphology. To test this, like we did in Section 4.1.3, we post a L_{bol} range cut on both AGN samples. Our conclusions do not change after doing the L_{bol} cut (the bottom panels of Figure 17). We have also checked that our conclusions will not change, if we do the faint end cut only, i.e. $L_{bol} \geq 10^{44}$ erg/s. Nevertheless, we do notice that the distribution of X-ray AGNs seem to shift *slightly* towards bluer $(U-V)_{\rm corr}$ after excluding the faint X-ray AGNs, because the X-ray AGNs hosted by QGs are seemingly fainter than those hosted by SFGs (as already discussed in Section 4.1.2, also see Figure 22 below).

Finally, we compare normalized R_e of AGNs with non-AGNs. In order to remove the M_* and z dependence, each R_e is divided by the median R_e of a galaxy with the same M_* and at z. To do so, we adopt the galaxy mass-size relation measured by van der Wel et al. (2014), which was done for all 3D-HST+CANDELS galaxies at $z < 3$. In particular, we normalize R_e of individual galaxies in our sample with the best-fit M_*-R_e relation for *late-type* galaxies at the closest redshift bin of van der Wel et al. 2014 (see their Table 1). Because R_e in van der Wel et al. (2014) is the size of rest-frame 5000Å, we convert it to the size of H_{160} using the Equation (1) and (2) in van der Wel et al. (2014). Figure 18 shows distributions of normalized R_e for X-ray and IR AGNs, where X-ray AGNs are further divided into two subsamples according to star formation properties of host galaxies (Note that almost all IR AGNs are hosted by

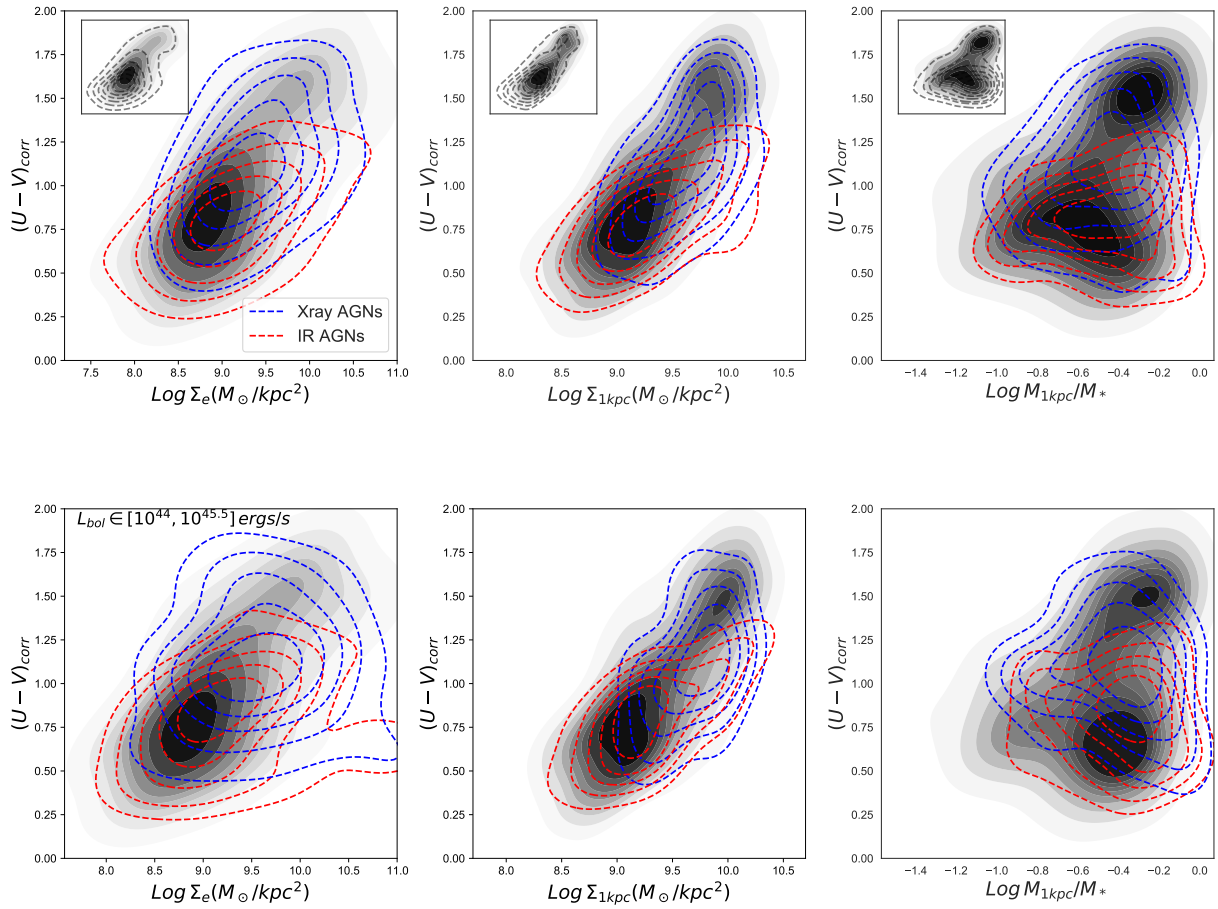

Figure 17. Upper: Distributions of AGNs (X-ray: blue, IR: red) and M_*-z matched non-AGNs (grey shades) in color-morphology diagrams. Number density distributions are estimated using the Gaussian kernel. For comparison, also plotted in the inserted sub-figure are the distributions of the entire sample of non-AGNs (grey lines) and the M_*-z matched subsample (grey shades). **Bottom:** Similar to the upper panels, but a L_{bol} range cut ($10^{44} - 10^{45.5}\,erg/s$) is posted on both AGN populations. Again, background grey contours show the distribution of non-AGNs whose M_* and z are matched to the L_{bol} cut AGN sample.

SFGs so we decide not to divide them into subsamples). The distribution of normalized R_e of IR AGNs shows that the sizes are in general consistent with sizes of normal SFGs, with a -0.07 dex median. Normalized R_e of X-ray AGNs hosted by SFGs are also consistent with normal SFGs, with a median and 16-84 percentile range of $-0.13^{+0.22}_{-0.37}$ dex, although it seems to be smaller than IR AGNs and skews to low normalized R_e. X-ray AGNs hosted by QGs have smaller normalized R_e, with a median and 16-84 percentile range of $-0.30^{+0.26}_{-0.31}$ dex. This is expected as QGs are in general more compact than SFGs at fixed M_*. If, instead, R_e of X-ray AGNs hosted by QGs is normalized with the best-fit M_*-R_e relation of van der Wel et al. (2014) for *early-type* galaxies (blue dashed curve in the Figure), normalized R_e changes to $+0.09^{+0.30}_{-0.27}$ dex, indicating that the sizes of X-ray AGN hosed by QGs are consistent with normal QGs.

4.2.2. *AGN prevalence vs. morphological properties*

We now investigate the dependence of q_{AGN} on M_*, Σ_e, Σ_{1kpc} and $\frac{M_{1kpc}}{M_*}$.

To begin, q_{AGN} increases with M_* (the left-most panel of Figure 19), the similar conclusion has also been made by many other authors (e.g. SDSS emission line selected AGNs: Kauffmann et al. 2003; X-ray AGNs: Xue et al. 2010; Aird et al. 2012). Given the well-known correlations among M_{BH}, bulge mass and M_*, the positive dependence of q_{AGN} on M_* is not surprising. Specifically speaking, an AGN is fueled by accretion onto a central SMBH, the rate and radiative efficiency of which together determine its luminosity. M_{BH} is positively and tightly correlated with bulge mass (see Kormendy & Ho 2013 and references therein) and, it is also positively (and likely superlinearly, Delvecchio et al. 2019) correlated with M_* although the correlation is not as

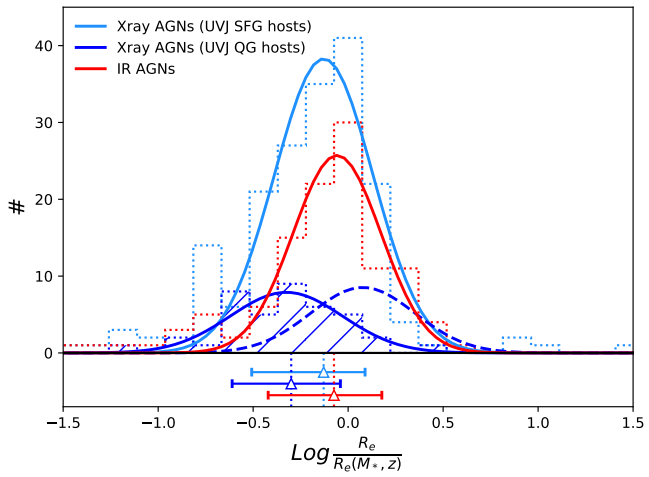

Figure 18. Distributions of normalized R_e of X-ray AGNs hosted by SFGs (light blue), X-ray AGNs hosted by QGs (blue) and IR AGNs (red). Each R_e is normalized with the best-fit M_*-R_e relation for normal *late-type* galaxies (taken from van der Wel et al. 2014). Solid lines are best-fit Gaussian distributions. Bottom panel shows medians and 16th-84th ranges of individual distributions. Blue dashed line shows the distribution of X-ray AGNs hosted QGs if we instead normalize R_e with the best-fit M_*-R_e relation for *early-type* galaxies.

tight as seen with bulge mass, (Reines & Volonteri 2015; Volonteri & Reines 2016; Savorgnan et al. 2016; Bentz & Manne-Nicholas 2018). Therefore, galaxies with larger M_* also statistically have larger M_{BH}, and hence tend to have higher *absolute* accretion rates (e.g. Mullaney et al. 2012; Yang et al. 2018). Given that AGNs are essentially selected according to some luminosity threshold, they are naturally expected to be more likely found in more massive galaxies. The positive trend between q_{AGN} and M_* is seen both for X-ray and IR AGNs, but with evidence that host galaxies of IR AGNs are less massive than those of X-ray AGNs. Combined with that IR AGNs are also more star-forming than X-ray AGNs (Figure 1 and Section 4.2.1), our findings for IR AGNs are consistent with Hickox & Boötes Survey Collaboration (2009) where they reported that IR AGN hosts are bluer and less massive than X-ray AGN hosts.

Also learnt from Figure 19 (middle two panels) is that q_{AGN} increases with stellar surface density, which is observed both for X-ray and IR AGNs. The q_{AGN}-Σ_{1kpc} trend could indicate that AGNs prevalently embed in galaxies with high Σ_{1kpc}, i.e. central compactness. Alternatively, the trend could be the "by-product" of the positive relations between q_{AGN} and M_* and, between M_* and Σ_{1kpc}. Since q_{AGN} increases with M_*, even without any intrinsic relation between q_{AGN} and galaxy central compactness, we still expect to see the increasing trend of q_{AGN} with Σ_{1kpc} (similar argument above can be used for Σ_e). In order to check if there is a causation between q_{AGN} and compactness of galaxies, instead of using the morphological metrics which are correlated with M_* like Σ_{1kpc} and Σ_e, we therefore look at the relation between q_{AGN} with $\frac{M_{1kpc}}{M_*}$ which has much weaker dependence on M_*.

As shown in the right-most panel of Figure 19, unlike increasing with M_* and Σ_{1kpc}, q_{AGN} stays more or less as a constant with $\frac{M_{1kpc}}{M_*}$, which again is observed for both X-ray and IR AGNs. The flat trend suggests that the probability of the presence of AGNs does not depend on galaxy compactness, i.e. no clear evidence on the prevalence of AGNs in compact galaxies. This, in return, indicates that the observed increasing trend between q_{AGN} and Σ_{1kpc} is *primarily* caused by the dependence of q_{AGN} on M_*, while the intrinsic connection (if any) between AGN and Σ_{1kpc} can only be the secondary. Similar conclusion has also been reached by Ni et al. (2019), where they found the sample-averaged BH accretion rate does not significantly depend on Σ_{1kpc} and Σ_e once SFR and M_* among galaxies are controlled.

Like what we did before (Section 4.1.3 and 4.2.1), we have checked, by posting a L_{bol} range cut on both AGN populations (the bottom panels of Figure 19) to ensure the X-ray and IR selections probe the similarly powerful AGNs, our conclusions above do not change.

Finally, we investigate if the relations seen above depend on star formation properties of host galaxies. This investigation is *only* conducted for X-ray AGNs because almost all IR AGN hosts are SFGs (see Figure 1). We first use UVJ-diagram to separate X-ray AGNs into two sub groups, namely SFGs and QGs. Figure 20 shows the dependence of q_{AGN} on each morphological parameter for X-ray AGNs hosted by UVJ-selected SFGs and QGs. While increasing trends between q_{AGN} and M_* are observed among both SFGs and QGs hosting X-ray AGNs, relations between q_{AGN} and Σ_{1kpc}, Σ_e depend on types of host galaxies. In particular, while SFGs hosting X-ray AGNs have the similar increasing trends between q_{AGN} and Σ_{1kpc}, Σ_e as observed for the entire sample of X-ray AGNs, flatter trends are observed for the ones hosted by QGs, which are consistent with the findings of Kocevski et al. (2017). For q_{AGN}-$\frac{M_{1kpc}}{M_*}$ relation, SFGs hosting X-ray AGNs show a flat trend, while QGs hosting X-ray AGNs seem to have a decreasing trend which however is far from conclusive at this point owing to the small sample size. We further test the findings by sub-grouping X-ray AGN hosts using R_{SB}. In this case, we divide the entire sample into four sub groups,

namely starburst (SB, $R_{SB} > 3$), main sequence (MS, $1/3 < R_{SB} < 3$), green valley (GV, $1/30 < R_{SB} < 1/3$) and QG ($R_{SB} < 1/30$). Like what we have seen when separating the sample with UVJ-diagram, except QG-hosting X-ray AGNs which show almost flat trend of q_{AGN} with Σ_e and Σ_{1kpc}, all other X-ray AGN hosts show the similar trends as seen for the entire X-ray AGN sample.

5. DISCUSSIONS

The main findings of this work can effectively be summarized by the scatter plot of Figure 22, where the M_*-dependence has been more or less removed for all shown parameters, including R_{SB} (y-axis), $\frac{M_{1kpc}}{M_*}$ (x-axis) and L_{bol}/M_* (point size). Despite the still relative large uncertainty in the L_{bol} measurement (Section 4.1.2), some general conclusions can be drawn. While there is no clear trend of L_{bol}/M_* with R_{SB} in the sample of SFGs hosting AGNs, the QGs hosting AGNs, which almost all come from the X-ray selection, appear to have overall lower L_{bol}/M_* than the SFGs hosting ones. Both X-ray and IR AGNs share similar $\frac{M_{1kpc}}{M_*}$ with normal SFGs, suggesting no clear link between galaxy compactness and the presences of AGNs. At the same time, although the median R_{SB} of X-ray AGNs is consistent with normal SFGs, its distribution is skewed to low R_{SB}. A different distribution of R_{SB} is observed for IR AGNs which generally have larger R_{SB} than normal SFGs. These show that the high incidence of AGNs being hosted by galaxies in the SFG-to-QG transitional region is *only* observed for X-ray AGNs, rather than for IR AGNs. In the following, we detail our discussions on how our findings can help constrain the effects of the AGN presences on galaxy quenching.

5.1. *Towards the general picture of AGN quenching*

While current cosmological simulations (e.g. Illustris (Vogelsberger et al. 2014), EAGLE (Schaller et al. 2015), IllustrisTNG (Pillepich et al. 2018), SIMBA (Davé et al. 2019)) can reproduce the observed statistics of massive galaxies by implementing AGN quenching of star formation, no consensus has yet emerged from the observations that such mechanism is effective in real galaxies.

Comparing star formation properties between AGNs and non-AGNs seems to be among the most straightforward tests. Our finding, that the median $sSFR/R_{SB}$ of AGNs is either similar to (X-ray AGNs) or larger than (IR AGNs) non-AGNs (Section 4.1.1), shows little evidence that the presence of an AGN suppresses the galaxy-wide star formation. Merely comparing the median/mean star formation properties of AGNs with non-AGNs may bias our view (Mullaney et al. 2015). A more detailed look shows that the distributions for X-ray AGN hosts are skewed to low $sSFR/R_{SB}$, which seemingly suggests a negative effect of AGNs on their hosts' star formation. However, because the similar distributions are *not* seen for IR AGNs, this calls into question whether the skewed distributions of star formation properties of X-ray AGNs are a manifestation of AGNs and quenching or simply an AGN selection effect. Similar results have also been obtained by Ellison et al. (2016), where they found that, compared with the M_*-z-environment matched non-AGNs, the SFR distributions of AGNs are different among different AGN selections. In particular, they found that their optical-selected AGNs have wide and skewed to low SFR distribution, while the distribution for their MIR-selected AGNs is skewed to high SFR (their Figure 3).

Similarly to what we found by comparing the distributions of star formation properties, we further study the relations of q_{AGN} with SFR, sSFR and R_{SB} (Section 4.1.3). While both X-ray AGNs and IR AGNs show higher incidence in galaxies with enhanced star formation relative to the main sequence, a higher incidence of X-ray AGNs is also seen in galaxies with suppressed star formation, which, however, *is not* seen in IR AGNs. Empirically speaking, any physical process that is observed to be preferentially taken place in the SFG-to-QG transitional phase may contain critical information of galaxy quenching (e.g. Strateva et al. 2001; Bell et al. 2004; Faber et al. 2007). While the over-abundance of X-ray AGNs is observed in galaxies with suppressed star formation, such conclusion certainly cannot be extrapolated to all AGNs, since we know that it is invalid for IR AGNs. We therefore conclude that the direct comparisons of the star formation properties between AGNs and non-AGNs show no clear evidence of a causal link between the presences of AGNs and galaxy quenching.

Next, if on-going AGN activities really were to play an observable role in affecting galaxy star formation properties, a correlation between AGN luminosities and star formation properties would be expected. In fact, a number of theoretical works predict the existence of a strong link between star formation and BH growth because both processes require cold gas supply (e.g. Di Matteo et al. 2005; Hopkins & Quataert 2010; Anglés-Alcázar et al. 2013). Regardless of the still relatively large measurement uncertainty, analysis in Section 4.1.2 shows null correlation between L_{bol} and R_{SB} in the SFG-hosting AGNs (both X-ray and IR), except that we see evidence that the brightest AGNs have the most intense star formation activities. These findings are fully aligned with other works (e.g. Lutz et al. 2008; Mullaney et al. 2012; Harrison et al. 2012), suggesting a rather weak/no

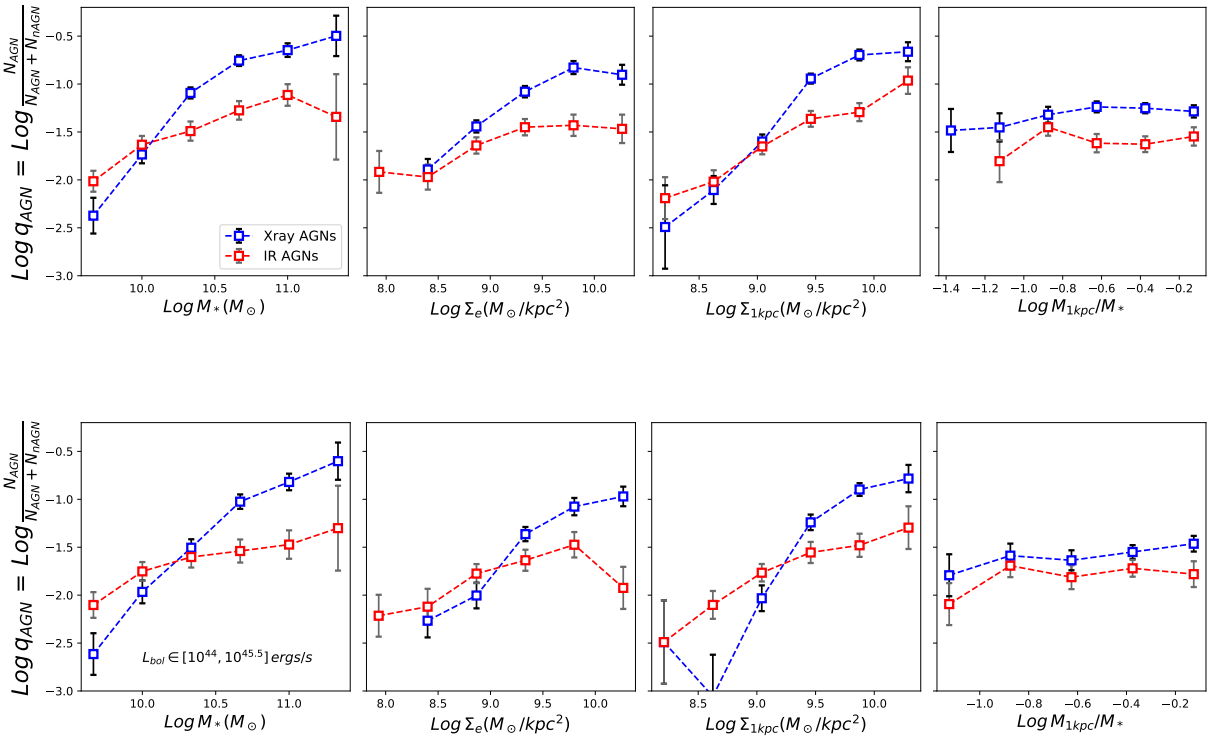

Figure 19. Similar to Figure 15. From left to right respectively: the dependence of q_{AGN} on M_*, Σ_e Σ_{1kpc} and $\frac{M_{1kpc}}{M_*}$.

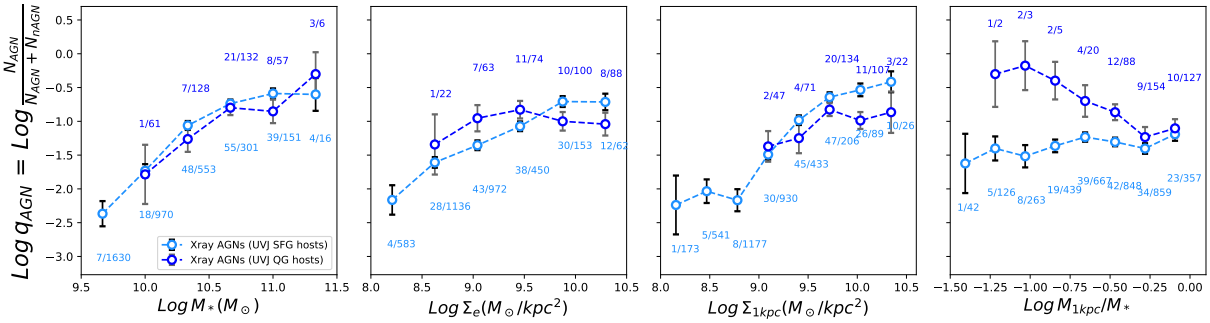

Figure 20. Similar to Figure 19. X-ray AGNs are divided into two sub groups based on star formation properties of their hosts, namely SFGs and QGs. The seemingly decreasing trend of q_{AGN} with $\frac{M_{1kpc}}{M_*}$ (the right-most panel) for X-ray AGNs hosted by QGs suffers from the small number statistics at the low-end of $\frac{M_{1kpc}}{M_*}$.

link between star formation and BH growth. However, because stochastic AGN variabilities can diminish the underlying strong star formation-BH correlation (Hickox et al. 2014) and, unfortunately, little is known about the AGN duty cycle, it is impossible to conclusively say the real cause(s) of the L_{bol}-R_{SB} null correlation.

While our understanding of the detailed physics driving galaxy quenching is still incomplete, theories suggest one possible evolutionary path, which has been shown by high resolution zoom-in simulations to be particularly effective in the early Universe when dissipative gas inflowing rate is high, namely that a galaxy undergoes a process of compaction as it transforming from a SFG to a QG (e.g. Zolotov et al. 2015; Tacchella et al. 2016). Some evidence supporting such mechanism has been reported based on recent observations, including the simi-

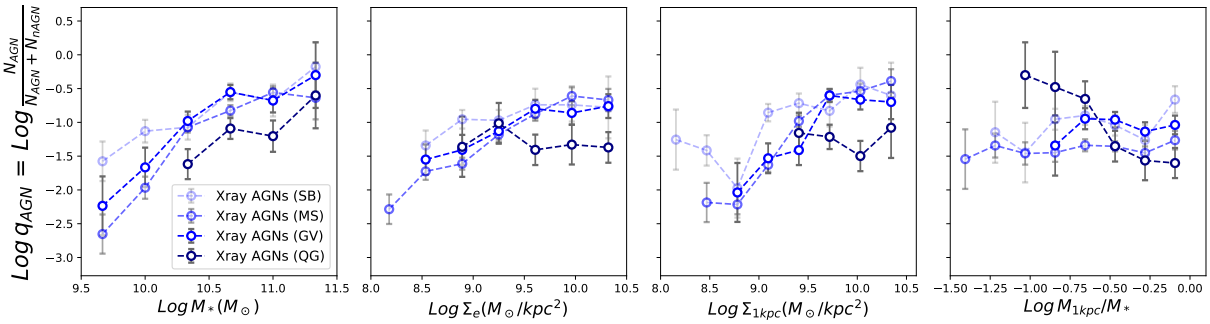

Figure 21. Similar to Figure 20, but X-ray AGN hosts are now divided based on their distances from SFMS R_{SB} (Section 4.1.2). In particular, X-ray AGNs are divided into 4 sub groups, namely starburst (SB), main sequence (MS), green valley (GV) and QG.

lar number densities, masses and sizes between compact SFGs and compact QGs (Barro et al. 2013), as well as the ALMA observed compact distribution of molecular gas and highly intense nucleated star formation activities in galaxies at $z \approx 2$ (e.g. Barro et al. 2016; Tadaki et al. 2017; Kaasinen et al. 2020). Similar to what has been reported by Kocevski et al. (2017), our analysis in Section 4.2.1 also finds a comparatively higher incidence of X-ray AGN hosts occupying a similar morphological parameter space as compact SFGs. This evidence seemingly suggests a causal link among the presence of an AGN, galaxy compaction and quenching. After adding IR AGNs to the same diagrams (Figure 16), however, we immediately realize that IR AGNs occupy the different parts of color-morphology space, namely to distribute more like normal SFGs, with similar $(U - V)_{corr}$, Σ_e and Σ_{1kpc}. These findings again question the claimed physical association between AGNs and galaxy quenching in the sense that the high incidence of AGNs being hosted by the SFG-to-QG transitional galaxies is only observed for X-ray AGNs and nor for IR AGNs. This significantly weakens the argument of that (X-ray) AGNs preferentially being hosted in compact SFGs is evidence of AGN quenching, since it depends on how the AGNs are selected and similar morphological characteristic of the host galaxies, i.e. frequent high compactness, is not observed for IR AGN hosts.

A further issue about the causal link between the presences of AGNs and galaxy compactness is noticed when we look at $\frac{M_{1kpc}}{M_*}$, the morphological parameter that we introduced as an alternative compactness metric (see Section 3.2.3 for details), which has the distinct advantage of the weak dependence on M_*. If $\frac{M_{1kpc}}{M_*}$ is used to define galaxy compactness, we see that not only IR AGNs but also X-ray AGNs have similar $\frac{M_{1kpc}}{M_*}$ distributions to normal SFGs' (Section 4.2.1 and the right most panels of Figure 16 and 17). This is different from the conclusions made upon the Σ_e and Σ_{1kpc} comparisons where X-ray AGNs seem to be more compact (larger Σ_e and Σ_{1kpc}) than normal SFGs. We remind that, however, our purpose here is not to argue which parameter is better in quantifying galaxy compactness. In fact, there is no universal definition of galaxy compactness and the physical meanings of Σ_e, Σ_{1kpc} and $\frac{M_{1kpc}}{M_*}$ obviously are all closely related. Depending on the specific analysis, we view the strong M_*-dependence of Σ_e and Σ_{1kpc} as a significant drawback when investigating the link between AGN activities and galaxy compactness, because the combination of the M_*-M_{BH} and M_*-$\Sigma_e(\Sigma_{1kpc})$ correlations can mimic a null correlation between AGN and galaxy compactness as a real one. This can be clearly seen in Section 4.2.2 where the relations of q_{AGN} with M_*, Σ_e, Σ_{1kpc} and $\frac{M_{1kpc}}{M_*}$ are studied. While q_{AGN} increases with M_*. Σ_e and Σ_{1kpc}, a flat trend is observed with $\frac{M_{1kpc}}{M_*}$ for both X-ray and IR AGNs, indicating that the higher incidence of AGN with larger Σ_{1kpc} is primarily due to M_* rather than a morphological reason. It is also possible that the q_{AGN}-Σ trends are driven by some other M_* surrogates, such as bulge fraction (B/T). As already mentioned in Section 3.2.2, we leave the relevant discussions of this possibility to a separate work.

Our combined study of X-ray and IR AGNs highlights the essential importance of AGN selection effects on the distributions of host galaxy properties. It is likely that different AGN selection methods are sensitive to different galaxy evolutionary states. In a simple BH-galaxy co-evolutionary model, one would expect a dusty BH growth, which tends to be picked up by IR observations, to occur in the early state of normal SFGs when both bulge and BH mass are built-up and to precede the less/un- obscured phase of BH growth that X-ray observations tend to pick up. Observational studies based on

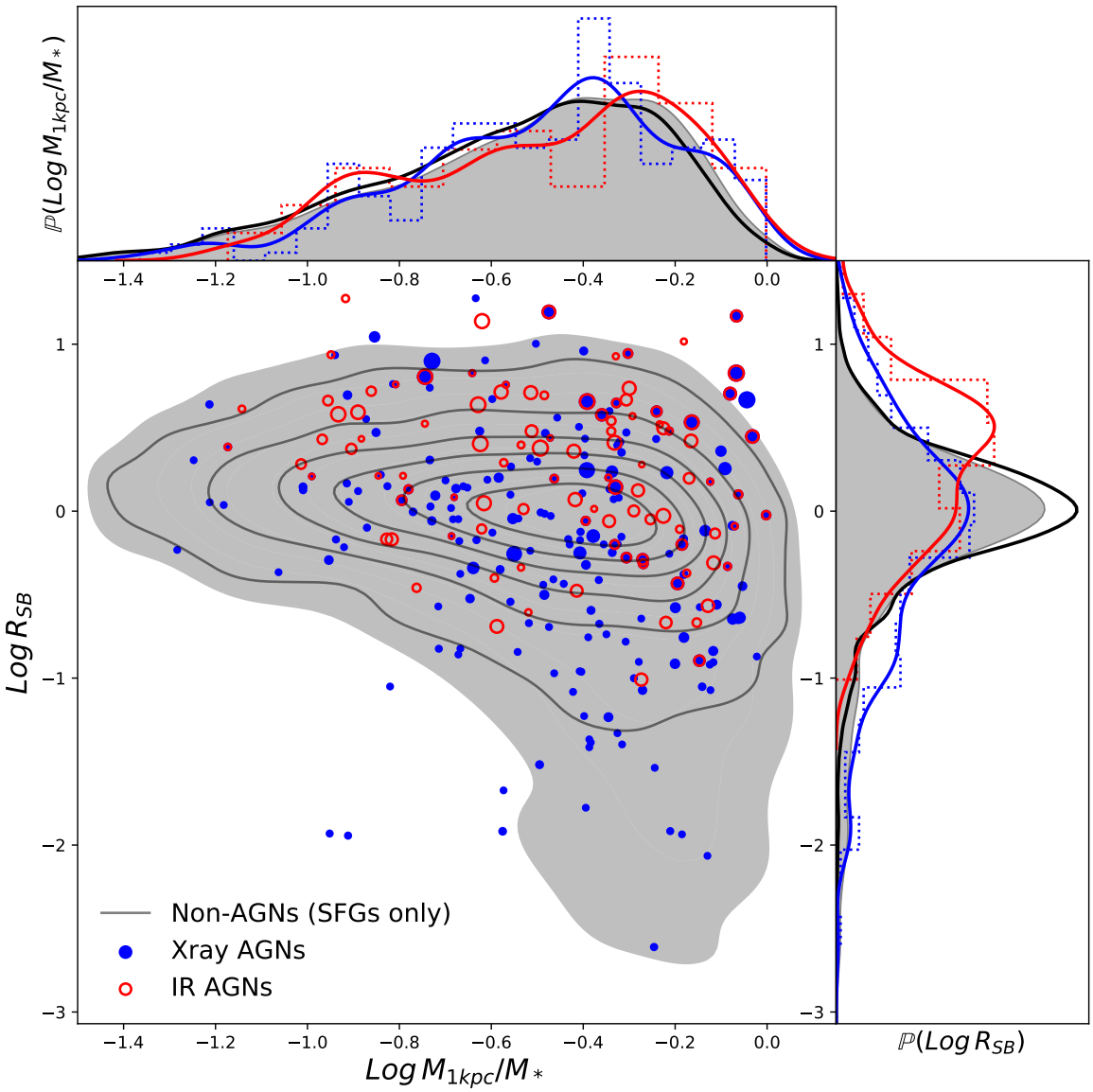

Figure 22. Distributions of AGNs and non-AGNs on the R_{SB}-$\frac{\mathrm{M_{1kpc}}}{\mathrm{M_*}}$ diagram. Black solid contours show the distribution of normal UVJ-selected SFGs, while the grey shaded contour shows the distribution for all non-AGNs (i.e. SFGs+QGs). X-ray and IR AGNs are shown as blue filled and red empty circles, sizes of which are scaled with L_{bol}/M_*. Also shown in the two sub-panels are the distributions of $\frac{\mathrm{M_{1kpc}}}{\mathrm{M_*}}$ and R_{SB} for different galaxy populations.

the host morphology of IR and X-ray selected AGNs find consistent results with this scenario. For example, Kocevski et al. (2015) argued that their IR selection preferentially selects obscured sources in SFGs before quenching has started, while X-ray selection preferentially finds unobscured sources after the central bulge has built-up and quenching has begun (see their Figure 10). The fact that we see IR AGNs live in galaxies like normal SFGs and X-ray AGNs live in transitional galaxies is in agreement with this simple evolutionary picture. A direct way to test this scenario would be to obtain high quality measurements of ages and BH accretion histories in the AGN hosts and then compare the differences between different AGN populations, which is the subject of our currently investigation. Since SFGs evolve by growing their stellar mass along the SFMS, however, a simplified version of this test would be to fix the SSFR and use the average $\mathrm{M_*}$ as a crude proxy for the age of the stellar populations. Figure 23 shows that, at fixed SSFR, IR AGN hosts are systematically less massive than X-

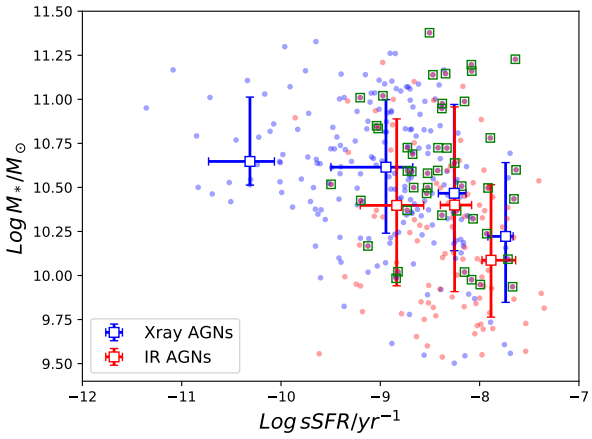

Figure 23. Median M_* at fixed SSFR of X-ray (blue) and IR (red) AGNs. Green squares mark the AGNs both selected by X-ray and IR.

ray AGN ones, supporting the idea that IR AGNs are observed at a younger stage, which is consistent with the BH-galaxy co-evolutionary model above. Therefore, the findings of this work certainly are not in direct conflict with AGN quenching, i.e. the scenario that AGNs drive the quenching of star formation in massive galaxies. On the other hand, however, the incidence of AGNs hosted by transitional galaxies, namely those with suppressed star formation and larger central surface mass density, depends on how the AGNs are selected. Thus, the fact that X-ray AGNs are preferentially hosted in transitional galaxies cannot be used as evidence of AGN quenching either, because this could also be simply a reflection of unobscured AGNs being more likely to show up during the later, less obscured evolutionary stages of the host without them having anything to do with the quenching of the host.

5.2. *Outlook for future studies – Combining all radiative AGNs selected by different methods*

Our discussions so far have treated X-ray and IR AGNs as two separate populations. Ideally, they should be combined as a single AGN population to compare with their non-AGN counterparts to investigate if the presences of AGNs in general, no matter how they are selected, correlate with host properties. However, the task of combining different AGN populations is non-trivial.

Regarding AGN luminosities, different selection methods are not homogeneous, which, for example, can be seen in Figure 13 that our IR selection is not as sensitive as the X-ray selection for faint AGNs. While it remains difficult to use the existing IR data to push the IR selection to the similar faint limit as of X-ray selection, this issue of luminosity inhomogeneity among different AGN selections, hopefully, can be resolved, or at least greatly mitigated, once the MIR capabilities of JWST will be online (Rieke et al. 2019).

Since the timescale for a galaxy shining like an AGN is extremely short compared with the lifetime of the galaxy, the AGN is, in practice, an almost instantaneous event and thus the total number of AGNs expected in a given field and at a given epoch of the Universe (e.g. redshift intervals) should be statistically proportional to the timescale of AGN presences. As a result, if the timescales change with the phases (e.g. obscured and unobscured) of BH growths, simply adding different AGNs together means to give more weights to the phase with longer timescale. Because different AGN selection methods are sensitive to different BH growth phases, e.g. IR/X-ray selection for the obscured/unobscured AGNs, the distributions of the host properties for a simple combined AGN population are biased towards the AGN selection that corresponds to the AGN phase with the longer timescale. Instead of simply adding up all AGNs, if we could add different types of AGNs with weights of the inverse of the corresponding timescales, the bias, in principle, would be eliminated. This would rely on a comprehensive knowledge of AGN duty cycle, the information of which unfortunately remains dramatically missing both theoretically and observationally.

Moreover, it is well known that radiative AGNs can effectively, but are not limited to, be identified by MIR colors and X-ray. AGNs selected through other methods, e.g. optical emission lines (e.g. Agostino & Salim 2019) or MIR SED decompositions, also occupy a significant fraction of AGN populations (e.g. Delvecchio et al. 2017). Our work immediately shows that potentially biased conclusions can be made based on a specific AGN selection method. To draw a comprehensive picture of AGN effects on host galaxies, it is therefore crucial for future studies to include all AGNs selected by different methods.

6. CAVEATS

Finally, we mention the caveats of this work. First, we emphasize that conclusions above should only apply to luminous AGNs. The current MIR data only allows for identifying very bright IR AGNs. While the deep X-ray data push the detection limit to ≈ 1 dex fainter for X-ray AGNs (Figure 13), the identified AGNs are still relatively bright ones. It is unclear that how the fainter and unidentified AGNs can affect our conclusions. Second, the effects of dust obscuration on our conclusions remain to be tested. Dust gradient can affect the H_{160}

(≈ rest-frame V-band at z∼2) light profiles. If, statistically, X-ray and IR AGN hosting galaxies share similar dust gradient, then the results of this work should not be greatly affected. However, if there exists intrinsic difference of dust obscuration between the two AGN populations, our conclusions might be affected. Since the IR selection is more sensitive to highly obscured AGNs, we would expect IR AGNs to more likely be hosted by galaxies with more nucleated dust obscuration, which might be able to even completely bury the central light from starbursts/AGNs. This actually is consistent with what we see in Figure 7 (see Section 3.2.2 for details). However, it is unclear to what extent the potentially different dust distributions can affect our conclusions, particularly for the distinct color-morphology distributions seen between X-ray and IR AGNs. In particular, if a high column density of dust only exists along lines of sight with a very small opening angle such that little stellar light is "blocked", our results should stand. On the other hand, if the opening angle of the high column density dust is large that significant amount of central stellar light is "blocked", then the IR AGNs could be more (although we do not know how much more) compact than they are seen in the H_{160} images. It will soon be possible to use JWST high angular resolution imaging in MIR, which is much less affected by dust obscuration, to finally investigate this issue.

7. SUMMARY

In this work, we carry out a combined study of X-ray and IR AGNs at $z \approx 2$ and compare the star formation and morphological properties of AGN and non-AGN host galaxies. We show that the criteria used to select AGNs have profound impacts on the distributions of host galaxy properties.

With regard to star formation properties,

- while the distributions of star formation properties (sSFR and R_{SB}) for X-ray AGN hosts is skewed to low values, the medians are similar to normal (i.e. non-AGN) SFGs on the SFMS. A similar distribution is *not* seen for IR AGNs, which show enhanced star formation relative to galaxies on the SFMS (Section 4.1.1).
- large measurement uncertainty of L_{bol} notwithstanding, no clear trends, neither for X-ray AGNs nor for IR AGNs, are seen between L_{bol} and R_{SB} (Section 4.1.2)
- the trends of q_{AGN} with SFR, sSFR and R_{SB} show that, despite high incidence is seen for both X-ray and IR AGNs in galaxies with intense star formation, the incidence of X-ray AGNs is also high in galaxies with suppressed star formation (sSFR and R_{SB}), which however is *not* seen for IR AGNs (Section 4.1.3).

With regard to morphological properties,

- distributions of morphological properties of X-ray and IR AGN hosts are very different in the color-morphology space (Section 4.2.1). In particular, while X-ray AGN hosts tend to have green colors and large stellar surface mass densities (both Σ_e and Σ_{1kpc}), IR AGN hosts show distributions that are much more similar to those of normal SFGs. Because both Σ_e and Σ_{1kpc} are strongly correlated with M_*, we introduce a new diagnostic of compactness $\frac{M_{1kpc}}{M_*}$, that significantly eliminates the dependence on M_*. We show that the distributions of $\frac{M_{1kpc}}{M_*}$ for both X-ray and IR AGNs are similar to normal SFGs'. Consistent results are also obtained by comparing the distribution of *normalized* R_e between AGNs and non-AGNs.
- increasing trends of q_{AGN} with Σ_e and Σ_{1kpc} are seen for both X-ray and IR AGN hosts. The trends with $\frac{M_{1kpc}}{M_*}$, however, remain more or less flat, indicating that the correlation with Σ_e and Σ_{1kpc} are primarily driven by M_* (Section 4.2.2).

While the findings presented above are not in direct conflict with the scenario of AGNs driving the quenching of massive galaxies, they do not support it either. Our findings show that the frequency of AGNs hosted by transitional (from SFGs to QGs) galaxies, namely galaxies with suppressed star formation and large surface stellar mass density, depends crucially on how the AGNs are selected. Thus, this calls into question the notion that there is a causal relationship between the presences of AGNs and the quenching of star formation. In fact, interpreting the different physical properties between the two AGN population hosts as evidence of different evolutionary phases of their ISM obscuration, for example, could imply another, yet unidentified, mechanism responsible for both quenching and the apparent evolution of the AGN properties.

1 We thank the anonymous referee for useful comments.
2 AK and CH gratefully acknowledge support from the
3 NASA/FINESST award (PID:19-ASTRO20-0078).

REFERENCES

Agostino, C. J., & Salim, S. 2019, ApJ, 876, 12, doi: 10.3847/1538-4357/ab1094

Aird, J., Coil, A. L., & Georgakakis, A. 2019, MNRAS, 484, 4360, doi: 10.1093/mnras/stz125

Aird, J., Coil, A. L., Moustakas, J., et al. 2012, ApJ, 746, 90, doi: 10.1088/0004-637X/746/1/90
Alexander, D. M., & Hickox, R. C. 2012, NewAR, 56, 93, doi: 10.1016/j.newar.2011.11.003
Anglés-Alcázar, D., Özel, F., & Davé, R. 2013, ApJ, 770, 5, doi: 10.1088/0004-637X/770/1/5
Armus, L., Charmandaris, V., Bernard-Salas, J., et al. 2007, ApJ, 656, 148, doi: 10.1086/510107
Azadi, M., Coil, A. L., Aird, J., et al. 2017, ApJ, 835, 27, doi: 10.3847/1538-4357/835/1/27
Barger, A. J., Cowie, L. L., Bauer, F. E., & González-López, J. 2019, ApJ, 887, 23, doi: 10.3847/1538-4357/ab5116
Barger, A. J., Cowie, L. L., Owen, F. N., et al. 2015, ApJ, 801, 87, doi: 10.1088/0004-637X/801/2/87
Barger, A. J., Cowie, L. L., Capak, P., et al. 2003, AJ, 126, 632, doi: 10.1086/376843
Barro, G., Faber, S. M., Pérez-González, P. G., et al. 2013, ApJ, 765, 104, doi: 10.1088/0004-637X/765/2/104
Barro, G., Kriek, M., Pérez-González, P. G., et al. 2016, ApJL, 827, L32, doi: 10.3847/2041-8205/827/2/L32
Barro, G., Faber, S. M., Koo, D. C., et al. 2017, ApJ, 840, 47, doi: 10.3847/1538-4357/aa6b05
Bell, E. F., Wolf, C., Meisenheimer, K., et al. 2004, ApJ, 608, 752, doi: 10.1086/420778
Bentz, M. C., & Manne-Nicholas, E. 2018, ApJ, 864, 146, doi: 10.3847/1538-4357/aad808
Berta, S., Lutz, D., Santini, P., et al. 2013, A&A, 551, A100, doi: 10.1051/0004-6361/201220859
Booth, C. M., & Schaye, J. 2009, MNRAS, 398, 53, doi: 10.1111/j.1365-2966.2009.15043.x
Brandt, W. N., & Alexander, D. M. 2015, A&A Rv, 23, 1, doi: 10.1007/s00159-014-0081-z
Brown, A., Nayyeri, H., Cooray, A., et al. 2019, ApJ, 871, 87, doi: 10.3847/1538-4357/aaf73b
Bruzual, G., & Charlot, S. 2003, MNRAS, 344, 1000, doi: 10.1046/j.1365-8711.2003.06897.x
Calzetti, D., Armus, L., Bohlin, R. C., et al. 2000, ApJ, 533, 682, doi: 10.1086/308692
Chabrier, G. 2003, PASP, 115, 763, doi: 10.1086/376392
Charlot, S., & Fall, S. M. 2000, ApJ, 539, 718, doi: 10.1086/309250
Ciesla, L., Charmandaris, V., Georgakakis, A., et al. 2015, A&A, 576, A10, doi: 10.1051/0004-6361/201425252
Ciotti, L., & Bertin, G. 1999, A&A, 352, 447
Cisternas, M., Jahnke, K., Bongiorno, A., et al. 2011, ApJL, 741, L11, doi: 10.1088/2041-8205/741/1/L11
Coil, A. L., Georgakakis, A., Newman, J. A., et al. 2009, ApJ, 701, 1484, doi: 10.1088/0004-637X/701/2/1484
Cowley, M. J., Spitler, L. R., Tran, K.-V. H., et al. 2016, MNRAS, 457, 629, doi: 10.1093/mnras/stv2992
da Cunha, E., Charlot, S., & Elbaz, D. 2008, MNRAS, 388, 1595, doi: 10.1111/j.1365-2966.2008.13535.x
Daddi, E., Alexander, D. M., Dickinson, M., et al. 2007, ApJ, 670, 173, doi: 10.1086/521820
Dahlen, T., Mobasher, B., Faber, S. M., et al. 2013, ApJ, 775, 93, doi: 10.1088/0004-637X/775/2/93
Davé, R., Anglés-Alcázar, D., Narayanan, D., et al. 2019, MNRAS, 486, 2827, doi: 10.1093/mnras/stz937
Delvecchio, I., Gruppioni, C., Pozzi, F., et al. 2014, MNRAS, 439, 2736, doi: 10.1093/mnras/stu130
Delvecchio, I., Smolčić, V., Zamorani, G., et al. 2017, A&A, 602, A3, doi: 10.1051/0004-6361/201629367
Delvecchio, I., Daddi, E., Shankar, F., et al. 2019, ApJL, 885, L36, doi: 10.3847/2041-8213/ab4e21
Delvecchio, I., Daddi, E., Aird, J., et al. 2020, ApJ, 892, 17, doi: 10.3847/1538-4357/ab789c
Di Matteo, T., Springel, V., & Hernquist, L. 2005, Nature, 433, 604, doi: 10.1038/nature03335
Donley, J. L., Rieke, G. H., Pérez-González, P. G., & Barro, G. 2008, ApJ, 687, 111, doi: 10.1086/591510
Donley, J. L., Koekemoer, A. M., Brusa, M., et al. 2012, ApJ, 748, 142, doi: 10.1088/0004-637X/748/2/142
Donley, J. L., Kartaltepe, J., Kocevski, D., et al. 2018, ApJ, 853, 63, doi: 10.3847/1538-4357/aa9ffa
Eisenhardt, P. R. M., Wu, J., Tsai, C.-W., et al. 2012, ApJ, 755, 173, doi: 10.1088/0004-637X/755/2/173
Eisenstein, D. J., Zehavi, I., Hogg, D. W., et al. 2005, ApJ, 633, 560, doi: 10.1086/466512
Ellison, S. L., Teimoorinia, H., Rosario, D. J., & Mendel, J. T. 2016, MNRAS, 458, L34, doi: 10.1093/mnrasl/slw012
Faber, S. M., Willmer, C. N. A., Wolf, C., et al. 2007, ApJ, 665, 265, doi: 10.1086/519294
Fabian, A. C. 2012, ARA&A, 50, 455, doi: 10.1146/annurev-astro-081811-125521
Feltre, A., Hatziminaoglou, E., Fritz, J., & Franceschini, A. 2012, MNRAS, 426, 120, doi: 10.1111/j.1365-2966.2012.21695.x
Fontanot, F., Pasquali, A., De Lucia, G., et al. 2011, MNRAS, 413, 957, doi: 10.1111/j.1365-2966.2010.18186.x
Fornasini, F. M., Civano, F., Fabbiano, G., et al. 2018, ApJ, 865, 43, doi: 10.3847/1538-4357/aada4e
Fritz, J., Franceschini, A., & Hatziminaoglou, E. 2006, MNRAS, 366, 767, doi: 10.1111/j.1365-2966.2006.09866.x
Giavalisco, M., Ferguson, H. C., Koekemoer, A. M., et al. 2004, ApJL, 600, L93, doi: 10.1086/379232
Gilli, R., Comastri, A., & Hasinger, G. 2007, A&A, 463, 79, doi: 10.1051/0004-6361:20066334

Graham, A. W., & Driver, S. P. 2005, PASA, 22, 118, doi: 10.1071/AS05001
Grogin, N. A., Kocevski, D. D., Faber, S. M., et al. 2011, ApJS, 197, 35, doi: 10.1088/0067-0049/197/2/35
Guo, Y., Ferguson, H. C., Giavalisco, M., et al. 2013, ApJS, 207, 24, doi: 10.1088/0067-0049/207/2/24
Haehnelt, M. G., Natarajan, P., & Rees, M. J. 1998, MNRAS, 300, 817, doi: 10.1046/j.1365-8711.1998.01951.x
Hainline, K. N., Reines, A. E., Greene, J. E., & Stern, D. 2016, ApJ, 832, 119, doi: 10.3847/0004-637X/832/2/119
Harrison, C. M., Alexander, D. M., Mullaney, J. R., et al. 2012, ApJL, 760, L15, doi: 10.1088/2041-8205/760/1/L15
Hasinger, G., Miyaji, T., & Schmidt, M. 2005, A&A, 441, 417, doi: 10.1051/0004-6361:20042134
Hatton, S., Devriendt, J. E. G., Ninin, S., et al. 2003, MNRAS, 343, 75, doi: 10.1046/j.1365-8711.2003.05589.x
Hatziminaoglou, E., Omont, A., Stevens, J. A., et al. 2010, A&A, 518, L33, doi: 10.1051/0004-6361/201014679
Hickox, R. C., & Boötes Survey Collaboration. 2009, in Astronomical Society of the Pacific Conference Series, Vol. 408, The Starburst-AGN Connection, ed. W. Wang, Z. Yang, Z. Luo, & Z. Chen, 341
Hickox, R. C., Mullaney, J. R., Alexander, D. M., et al. 2014, ApJ, 782, 9, doi: 10.1088/0004-637X/782/1/9
Hopkins, P. F., & Quataert, E. 2010, MNRAS, 407, 1529, doi: 10.1111/j.1365-2966.2010.17064.x
Hopkins, P. F., Richards, G. T., & Hernquist, L. 2007, ApJ, 654, 731, doi: 10.1086/509629
Hopkins, P. F., Somerville, R. S., Hernquist, L., et al. 2006, ApJ, 652, 864, doi: 10.1086/508503
Hsu, L.-T., Salvato, M., Nandra, K., et al. 2014, ApJ, 796, 60, doi: 10.1088/0004-637X/796/1/60
Ji, Z., Giavalisco, M., Williams, C. C., et al. 2018, ApJ, 862, 135, doi: 10.3847/1538-4357/aacc2c
Ji, Z., Giavalisco, M., Vanzella, E., et al. 2020, ApJ, 888, 109, doi: 10.3847/1538-4357/ab5fdc
Kaasinen, M., Walter, F., Novak, M., et al. 2020, ApJ, 899, 37, doi: 10.3847/1538-4357/aba438
Kartaltepe, J. S., Sanders, D. B., Le Floc'h, E., et al. 2010, ApJ, 721, 98, doi: 10.1088/0004-637X/721/1/98
Kauffmann, G., Heckman, T. M., White, S. D. M., et al. 2003, MNRAS, 341, 33, doi: 10.1046/j.1365-8711.2003.06291.x
Kaviraj, S., Martin, G., & Silk, J. 2019, MNRAS, 489, L12, doi: 10.1093/mnrasl/slz102
Kaviraj, S., Laigle, C., Kimm, T., et al. 2017, MNRAS, 467, 4739, doi: 10.1093/mnras/stx126
Kirkpatrick, A., Pope, A., Alexander, D. M., et al. 2012, ApJ, 759, 139, doi: 10.1088/0004-637X/759/2/139
Kirkpatrick, A., Pope, A., Charmandaris, V., et al. 2013, ApJ, 763, 123, doi: 10.1088/0004-637X/763/2/123
Kirkpatrick, A., Alberts, S., Pope, A., et al. 2017, ApJ, 849, 111, doi: 10.3847/1538-4357/aa911d
Kocevski, D. D., Faber, S. M., Mozena, M., et al. 2012, ApJ, 744, 148, doi: 10.1088/0004-637X/744/2/148
Kocevski, D. D., Brightman, M., Nandra, K., et al. 2015, ApJ, 814, 104, doi: 10.1088/0004-637X/814/2/104
Kocevski, D. D., Barro, G., Faber, S. M., et al. 2017, ApJ, 846, 112, doi: 10.3847/1538-4357/aa8566
Koekemoer, A. M., Faber, S. M., Ferguson, H. C., et al. 2011, ApJS, 197, 36, doi: 10.1088/0067-0049/197/2/36
Kormendy, J., & Ho, L. C. 2013, ARA&A, 51, 511, doi: 10.1146/annurev-astro-082708-101811
Lacy, M., Storrie-Lombardi, L. J., Sajina, A., et al. 2004, ApJS, 154, 166, doi: 10.1086/422816
Law, D. R., Steidel, C. C., Shapley, A. E., et al. 2012, ApJ, 745, 85, doi: 10.1088/0004-637X/745/1/85
Lee, B., Giavalisco, M., Whitaker, K., et al. 2018, ApJ, 853, 131, doi: 10.3847/1538-4357/aaa40f
Leja, J., Carnall, A. C., Johnson, B. D., Conroy, C., & Speagle, J. S. 2019, ApJ, 876, 3, doi: 10.3847/1538-4357/ab133c
Leung, G. C. K., Coil, A. L., Azadi, M., et al. 2017, ApJ, 849, 48, doi: 10.3847/1538-4357/aa9024
Liu, T., Tozzi, P., Wang, J.-X., et al. 2017, ApJS, 232, 8, doi: 10.3847/1538-4365/aa7847
Lotz, J. M., Primack, J., & Madau, P. 2004, AJ, 128, 163, doi: 10.1086/421849
Luo, B., Brandt, W. N., Xue, Y. Q., et al. 2017, ApJS, 228, 2, doi: 10.3847/1538-4365/228/1/2
Lutz, D., Sturm, E., Tacconi, L. J., et al. 2008, ApJ, 684, 853, doi: 10.1086/590367
Lutz, D., Mainieri, V., Rafferty, D., et al. 2010, ApJ, 712, 1287, doi: 10.1088/0004-637X/712/2/1287
Madau, P., & Dickinson, M. 2014, ARA&A, 52, 415, doi: 10.1146/annurev-astro-081811-125615
Marleau, F. R., Clancy, D., Habas, R., & Bianconi, M. 2017, A&A, 602, A28, doi: 10.1051/0004-6361/201629832
Martin, D. C., Wyder, T. K., Schiminovich, D., et al. 2007, ApJS, 173, 342, doi: 10.1086/516639
Mendez, A. J., Coil, A. L., Aird, J., et al. 2016, ApJ, 821, 55, doi: 10.3847/0004-637X/821/1/55
Mihos, J. C., & Hernquist, L. 1996, ApJ, 464, 641, doi: 10.1086/177353
Mullaney, J. R., Daddi, E., Béthermin, M., et al. 2012, ApJL, 753, L30, doi: 10.1088/2041-8205/753/2/L30
Mullaney, J. R., Alexander, D. M., Aird, J., et al. 2015, MNRAS, 453, L83, doi: 10.1093/mnrasl/slv110

Nandra, K., Georgakakis, A., Willmer, C. N. A., et al. 2007, ApJL, 660, L11, doi: 10.1086/517918
Newman, A. B., Ellis, R. S., Bundy, K., & Treu, T. 2012, ApJ, 746, 162, doi: 10.1088/0004-637X/746/2/162
Ng, P., & Maechler, M. 2007, Statistical Modelling, 7, 315
Ng, P. T., & Maechler, M. 2020, COBS – Constrained B-splines (Sparse matrix based)
Ni, Q., Yang, G., Brandt, W. N., et al. 2019, MNRAS, 490, 1135, doi: 10.1093/mnras/stz2623
Oppenheimer, B. D., Davé, R., Kereš, D., et al. 2010, MNRAS, 406, 2325, doi: 10.1111/j.1365-2966.2010.16872.x
Page, M. J., Symeonidis, M., Vieira, J. D., et al. 2012, Nature, 485, 213, doi: 10.1038/nature11096
Peirani, S., Dubois, Y., Volonteri, M., et al. 2017, MNRAS, 472, 2153, doi: 10.1093/mnras/stx2099
Peng, C. Y., Ho, L. C., Impey, C. D., & Rix, H.-W. 2010, AJ, 139, 2097, doi: 10.1088/0004-6256/139/6/2097
Petrosian, V. 1976, ApJL, 209, L1, doi: 10.1086/182253
Pillepich, A., Springel, V., Nelson, D., et al. 2018, MNRAS, 473, 4077, doi: 10.1093/mnras/stx2656
Planck Collaboration, Ade, P. A. R., Aghanim, N., et al. 2016, A&A, 594, A13, doi: 10.1051/0004-6361/201525830
Pope, A., Chary, R.-R., Alexander, D. M., et al. 2008, ApJ, 675, 1171, doi: 10.1086/527030
Reines, A. E., & Volonteri, M. 2015, ApJ, 813, 82, doi: 10.1088/0004-637X/813/2/82
Rieke, G., Alberts, S., Shivaei, I., Colina, L., & Nørgaard-Nielsen, H. U. 2019, BAAS, 51, 11
Rieke, G. H., Alonso-Herrero, A., Weiner, B. J., et al. 2009, ApJ, 692, 556, doi: 10.1088/0004-637X/692/1/556
Rodighiero, G., Brusa, M., Daddi, E., et al. 2015, ApJL, 800, L10, doi: 10.1088/2041-8205/800/1/L10
Rosario, D. J., Santini, P., Lutz, D., et al. 2012, A&A, 545, A45, doi: 10.1051/0004-6361/201219258
Rovilos, E., Comastri, A., Gilli, R., et al. 2012, A&A, 546, A58, doi: 10.1051/0004-6361/201218952
Salim, S., Rich, R. M., Charlot, S., et al. 2007, ApJS, 173, 267, doi: 10.1086/519218
Sanders, D. B., Soifer, B. T., Elias, J. H., et al. 1988, ApJ, 325, 74, doi: 10.1086/165983
Santini, P., Rosario, D. J., Shao, L., et al. 2012, A&A, 540, A109, doi: 10.1051/0004-6361/201118266
Satyapal, S., Ellison, S. L., McAlpine, W., et al. 2014, MNRAS, 441, 1297, doi: 10.1093/mnras/stu650
Savorgnan, G. A. D., Graham, A. W., Marconi, A., & Sani, E. 2016, ApJ, 817, 21, doi: 10.3847/0004-637X/817/1/21
Schaller, M., Dalla Vecchia, C., Schaye, J., et al. 2015, MNRAS, 454, 2277, doi: 10.1093/mnras/stv2169
Schawinski, K., Urry, C. M., Virani, S., et al. 2010, ApJ, 711, 284, doi: 10.1088/0004-637X/711/1/284
Schreiber, C., Pannella, M., Elbaz, D., et al. 2015, A&A, 575, A74, doi: 10.1051/0004-6361/201425017
Silk, J., & Rees, M. J. 1998, A&A, 331, L1. https://arxiv.org/abs/astro-ph/9801013
Silverman, J. D., Mainieri, V., Salvato, M., et al. 2010, ApJS, 191, 124, doi: 10.1088/0067-0049/191/1/124
Somerville, R. S., & Davé, R. 2015, ARA&A, 53, 51, doi: 10.1146/annurev-astro-082812-140951
Stanley, F., Harrison, C. M., Alexander, D. M., et al. 2015, MNRAS, 453, 591, doi: 10.1093/mnras/stv1678
Stern, D., Eisenhardt, P., Gorjian, V., et al. 2005, ApJ, 631, 163, doi: 10.1086/432523
Stern, D., Assef, R. J., Benford, D. J., et al. 2012, ApJ, 753, 30, doi: 10.1088/0004-637X/753/1/30
Strateva, I., Ivezić, Ž., Knapp, G. R., et al. 2001, AJ, 122, 1861, doi: 10.1086/323301
Tacchella, S., Dekel, A., Carollo, C. M., et al. 2016, MNRAS, 458, 242, doi: 10.1093/mnras/stw303
Tadaki, K.-i., Genzel, R., Kodama, T., et al. 2017, ApJ, 834, 135, doi: 10.3847/1538-4357/834/2/135
Treister, E., Schawinski, K., Urry, C. M., & Simmons, B. D. 2012, ApJL, 758, L39, doi: 10.1088/2041-8205/758/2/L39
Tremonti, C. A., Heckman, T. M., Kauffmann, G., et al. 2004, ApJ, 613, 898, doi: 10.1086/423264
van der Wel, A., Bell, E. F., Häussler, B., et al. 2012, ApJS, 203, 24, doi: 10.1088/0067-0049/203/2/24
van der Wel, A., Franx, M., van Dokkum, P. G., et al. 2014, ApJ, 788, 28, doi: 10.1088/0004-637X/788/1/28
Villforth, C., Hamann, F., Rosario, D. J., et al. 2014, MNRAS, 439, 3342, doi: 10.1093/mnras/stu173
Vogelsberger, M., Genel, S., Springel, V., et al. 2014, MNRAS, 444, 1518, doi: 10.1093/mnras/stu1536
Volonteri, M., & Reines, A. E. 2016, ApJL, 820, L6, doi: 10.3847/2041-8205/820/1/L6
Wang, E., Kong, X., & Pan, Z. 2018, ApJ, 865, 49, doi: 10.3847/1538-4357/aadb9e
Wechsler, R. H., & Tinker, J. L. 2018, ARA&A, 56, 435, doi: 10.1146/annurev-astro-081817-051756
Weinberger, R., Springel, V., Hernquist, L., et al. 2017, MNRAS, 465, 3291, doi: 10.1093/mnras/stw2944
Whitaker, K. E., Franx, M., Leja, J., et al. 2014, ApJ, 795, 104, doi: 10.1088/0004-637X/795/2/104
Williams, R. J., Quadri, R. F., Franx, M., van Dokkum, P., & Labbé, I. 2009, ApJ, 691, 1879, doi: 10.1088/0004-637X/691/2/1879
Xue, Y. Q., Luo, B., Brandt, W. N., et al. 2016, ApJS, 224, 15, doi: 10.3847/0067-0049/224/2/15

Xue, Y. Q., Brandt, W. N., Luo, B., et al. 2010, ApJ, 720, 368, doi: 10.1088/0004-637X/720/1/368

Yang, G., Chen, C.-T. J., Vito, F., et al. 2017, ApJ, 842, 72, doi: 10.3847/1538-4357/aa7564

Yang, G., Brandt, W. N., Vito, F., et al. 2018, MNRAS, 475, 1887, doi: 10.1093/mnras/stx2805

Zolotov, A., Dekel, A., Mandelker, N., et al. 2015, MNRAS, 450, 2327, doi: 10.1093/mnras/stv740

APPENDIX

A. TESTS OF SYSTEMATIC UNCERTAINTY WHEN USING LEE2018 SED FITTING MEASUREMENTS

We use SED3FIT to test that if neglecting the AGN component when carrying out SED fitting with the methodology of Lee2018 can introduce significant systematic bias into the physical parameters of the AGN sample. SED3FIT is built upon MAGPHYS (da Cunha et al. 2008) and includes an AGN component into the modeling. During the SED3FIT fitting, a galaxy's SED is modelled as the combination of stellar emission, dust emission (PAHs, hot dust and cold dust) and an user-defined AGN spectral library. The basic setup of SED3FIT is the same as MAGPHYS, namely using the BC03 stellar population synthesis code, assuming Chabrier (2003) IMF and Charlot & Fall (2000) dust attenuation model. SED3FIT uses a parametric SFH, which is assumed to be the summation of two components – an underlying exponential decline SFR(t) $\propto exp(-\gamma t)$ with random bursts superimposed. Given that the data coverage of each sample galaxy is limited (typical number of photometric bands is ≈ 15, $\approx 60\%$ of AGN samples also have MIPS/24μm data), we followed the same procedure as Delvecchio et al. (2014) to only adopt a subset of the AGN spectral library of Fritz et al. (2006) and Feltre et al. (2012). By testing with the mock galaxies hosting different types of AGNs (Type I, Type II or intermediate), Ciesla et al. (2015) showed that the derived parameters such as M_* and SFR are insensitive to the adopted AGN library.

A.1. *Stellar mass M_**

Figure 24 (a) shows comparisons of the M_* measurements between Lee2018 and SED3FIT. A clear correlation between the two M_* is seen for the AGN sample. An ≈ 0.2 dex offset between the two measurements is also seen, with M_* derived by SED3FIT being larger than that derived by Lee2018. This offset can be attributed to the different setups between the two SED-fitting procedures, either due to including the AGN component to the modelling, or due to other different assumptions on things like SFH and dust attenuation law which are not related to the presences of AGNs. To check this, we ran MAGPHYS over a subsample of normal galaxies whose M_* and redshift distributions are matched to the AGN sample. For each AGN, we select two normal galaxies who are closest to the AGN in the M_*-z space.

Like what is seen for the AGNs, an offset of the M_* measurements between Lee2018 and SED3FIT is also observed for the M_*-z-matched normal galaxies. Moreover, as the right panel of Figure 24 (a) shows, the magnitude of the offset seen for the non-AGNs (≈ 0.15 dex) is also similar as that seen for the AGNs (≈ 0.17 dex). These suggest that the offset between the two M_* measurements of our AGNs is primarily from the different assumptions *unrelated* to the presences of AGNs, very likely due to different assumptions on SFHs and dust reddening laws. This conclusion actually is not surprising given that the rest-frame UV to NIR SEDs are usually dominated by stellar light even when AGNs exist (see Section 4 in Brandt & Alexander 2015 and references therein). We have further tested the M_* measurements by looking at the relation between the M_* difference δLogM_* and AGN X-ray intrinsic luminosity taken from Xue et al. (2016) and Luo et al. (2017). If the AGN component plays a vital role in the determination of M_*, then we would expect to see a dependence of δLogM_* on AGN luminosity, which however is not seen in Figure 25. We therefore conclude that our M_* measurement using Lee2018 is robust.

Finally, we do notice that some (though a small fraction) AGNs have rather large deviations of M_* measurements between the two SED-fittings (both in Figure 24 and Figure 25). Santini et al. (2012) checked the robustness of their M_* measurements of Type 1 and Type 2 AGNs using two sets of SED fittings, one with the AGN component included while the other without. They found the M_* of Type 2 AGNs can be very well-constrained even without including the AGN component during their SED-fittings, with the mean difference in M_* measurements between the two SED-fittings being zero and only in 1.3% of objects the difference is larger than a factor of 2. For Type 1 AGNs, although the mean difference in M_* is still consistent with ≈ 0, the difference in 29% of objects is larger than a factor of 2. Similar results have also been found by other authors (e.g. Yang et al. 2018). Motivated by the potential different systematics between Type 1 and Type 2 AGNs, we have cross-matched our AGN sample with the broad-line (BL) X-ray AGNs in the GOODS-S (Silverman et al. 2010) and GOODS-N (Barger et al. 2003). 19 BL AGNs are found and marked as magenta open circles in Figure 24. We do find that a considerable number of AGNs with large differences in M_* measurements are BL AGNs. After comparing the difference of M_* measurements between BL AGNs and other AGNs, we reach the similar conclusion as Santini et al. (2012), namely that the mean M_* differences are

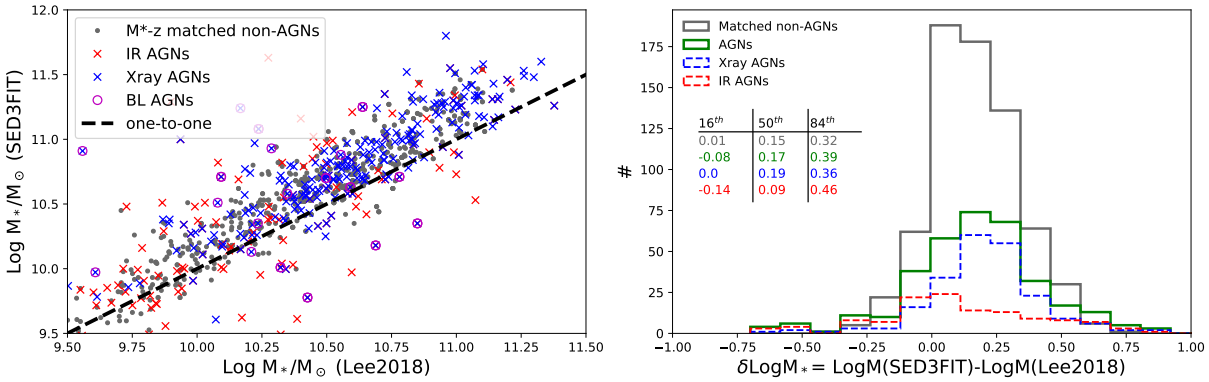

(a)

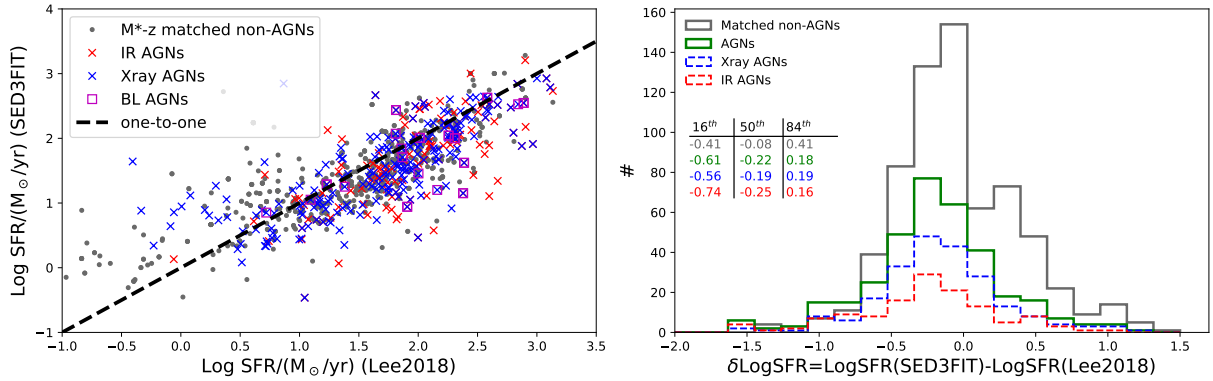

(b)

Figure 24. Comparisons between physical parameters derived from two SED-fitting procedures, namely Lee2018 and SED3FIT (see Section 3.1 for details). **(a) Left:** The comparison of M_* for the AGNs (green) and M_*-redshift matched normal galaxies (orange). BL AGNs are labelled with magenta open circles. The black dashed line marks the one-to-one relation. **Right:** Distributions of δLogM$_*$ for the AGNs (green) and non-AGNs (orange). The AGN sample has been further divided into X-ray AGNs (blue) and IR AGNs (red). Also tabulated are the 16th, 50th and 84th percentiles of the distributions. **(b):** Similar as (a) but for the comparison of SFR.

similar between BL and non-BL AGNs. The distribution of M_* difference of BL AGNs, however, is broader than that of non-BL AGNs, with the standard deviation of the former being larger than that of the latter by a factor of

$$\frac{\sigma(\delta \mathrm{M}_{*,\mathrm{BLAGNs}})}{\sigma(\delta \mathrm{M}_{*,\mathrm{nonBLAGNs}})} \approx \frac{0.53\,\mathrm{dex}}{0.28\,\mathrm{dex}} \approx 1.9. \tag{A1}$$

It is therefore important to properly model the AGN component to get good measures of M_* for BL AGNs, the detailed methodologies of which are beyond the scope of this work. We decide not to remove BL AGNs from our sample since they are a small fraction of the entire AGN sample and we have checked that our results are insensitive to including/excluding them.

A.2. *Star formation rate SFR*

Figure 24 (b) shows the comparison of SFRs between the two SED-fitting measurements. We refer readers to Lee2018 for a detailed discussion about the uncertainty of their SFR measurements using mock galaxies from semi-analytical simulations. A clear correlation between the two SFRs is observed both for the AGNs and the M_*-z matched non-AGNs, despite that the scatter is larger than in the case of the M_* comparison. The right panel of Figure 24 (b) compares the distributions of SFR difference between the AGNs and non-AGNs. Generally speaking, the two SED

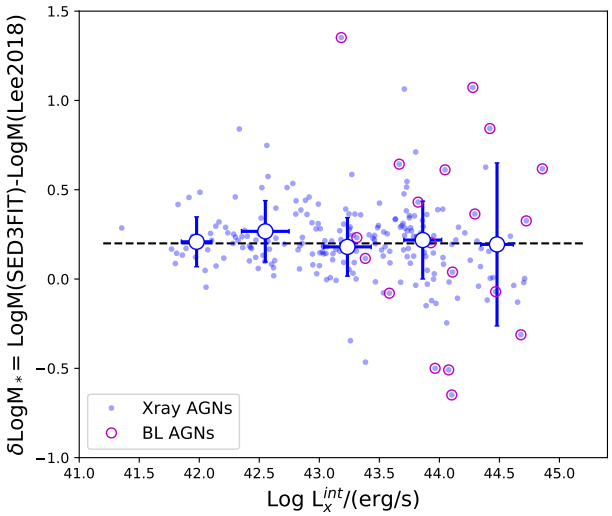

Figure 25. The relation between δLogM$_*$ and intrinsic X-ray luminosity. Blue dots are individual X-ray AGNs. In each X-ray luminosity bin, the mean and standard deviation of δLogM$_*$ is shown as a blue square with error bars. The median δLogM$_*$ of the entire sample is marked as the black dashed line. BL AGNs are labelled with magenta open circles.

procedures yield consistent estimates of SFRs for the non-AGNs, with a median δLogSFR = 0.08 dex. For the AGNs, SFRs from Lee2018 are on average larger than those from SED3FIT by 0.22 dex.

A closer look at the left panel of Figure 24 (b) shows that, unlike for galaxies with moderate/high SFRs, SED3FIT predicts larger SFRs than Lee2018 for galaxies with low SFRs, indicating different systematics of SFR measurements between SFGs and QGs. Such systematics are very likely due to the assumptions of SFHs. In Lee2018, they tested the SED-derived SFRs using mock galaxies (see their Figure 6), where they showed that an incorrect SFH can lead to significantly biased SFR measurements for QGs. Also in Leja et al. (2019), they showed that treating SFH as a free parameter is essential for the unbiased measurements of SFRs. While assumptions on the SFH can result in strong deviations of the SFR measurements from the intrinsic values for QGs, the situation for SFGs seems to be much better (see Figure 6 in Lee2018 for an example). Therefore, as Figure 26 shows, we only compare the SFRs between AGN hosted by SFGs and M$_*$-z matched normal SFGs (note that before we did not put any constrains on the star formation properties when building the M$_*$-z matched normal galaxies). Compared with Figure 24 (b), we find that the difference of δLogSFR between AGNs and non-AGNs decreases from ≈ 0.2 dex to ≈ 0.1 dex, which is much smaller than the 1σ range of entire distributions ($\gtrsim 0.7$ dex). Nevertheless, the remaining 0.1 dex difference between the two SED fittings is very likely due to neglecting the AGN component in Lee2018 fits.

In Figure 27, we also investigate the relation between δLogSFR and intrinsic X-ray luminosity. We do not see any clear trend except for the brightest bin ($L_X \sim 10^{44.5}$ ergs/s), where the over-estimation of SFR can be as large as $\approx$ 0.5 dex.

A.3. *Rest-frame colors*

The last parameters that we have checked are the rest-frame colors. We first compare the apparent (i.e. dust-attenuated) rest colors $U-V$ and $V-J$ derived from the two SED fittings. To do so, we convolve the best-fit spectra with the Bessel U, V and 2MASS J filters respectively. As the left two panels of Figure 28 shows, the apparent rest-frame colors derived from the two SED procedures are in very good agreement with each other. The distributions of AGNs on the UVJ diagram (Figure 1) therefore are not sensitive to the choice of the SED fitting procedure.

A more involved measurement is that of the dust-corrected rest-frame colors, i.e. colors that are corrected for dust attenuation (recall that Lee2018 assumes Calzetti et al. 2000 dust attenuation law and SED3FIT assumes Charlot & Fall 2000 model). The comparisons of the dust-corrected colors $(U-V)_{corr}$ and $(V-J)_{corr}$ are shown in the right panels of Figure 28. Unlike the dust-uncorrected colors, both systematic offsets and larger scatters between the two

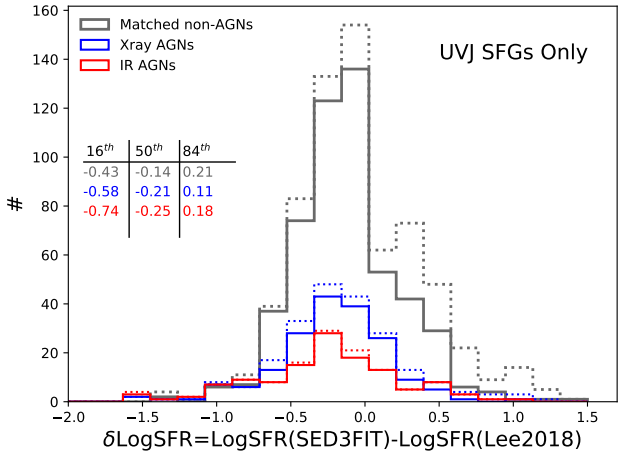

Figure 26. Similar to the right panel of Figure 24 (b), but the solid histograms show the results for SFGs only, i.e. AGNs hosted by SFGs and M_*-z matched normal SFGs. The histograms of Figure 24 (b) are also plotted (dotted) for comparison.

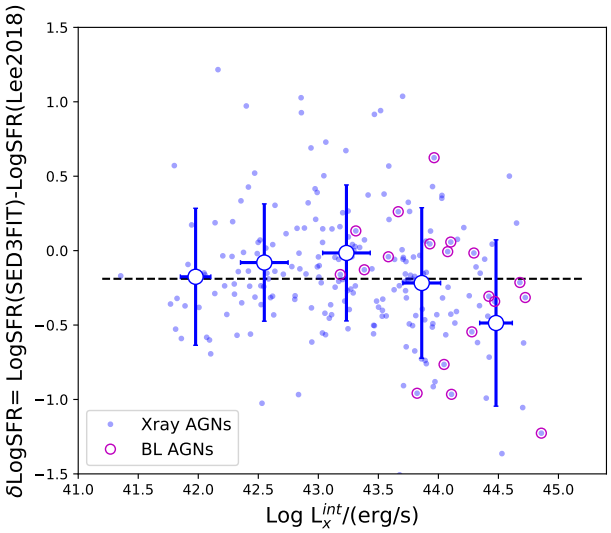

Figure 27. Similar to Figure 25 but for δLogSFR.

measurements are seen for the dust-corrected colors, which illustrate the essential role played by the assumed dust attenuation models when measuring the properties of stellar populations. For $(U-V)_{corr}$, similar offsets ($\approx 0.3 m_{AB}$) and scatters are seen for both AGNs and non-AGNs, which indicates that the differences between the two SED measurements are primarily driven by assumptions *unrelated* to the presences of AGNs. Similar conclusion can also be made for $(V-J)_{corr}$, although the scatters of IR AGNs seem to be larger than X-ray AGNs and non-AGNs, very likely because the AGN contribution to the J band is generally larger for IR AGNs than for X-ray AGNs (see Figure 3). We caution that, however, our conclusions, which are drawn based on the comparisons of rest-frame colors above, depend on correctness of the assumed AGN models. While the SEDs of Type 1 AGNs have been empirically well characterized at UV through NIR wavelengths, the situation for the fainter Type 2 AGN in general, such as the majority considered here, is more uncertain. While significant progress has been made to observationally constrain the SEDs of faint AGNs

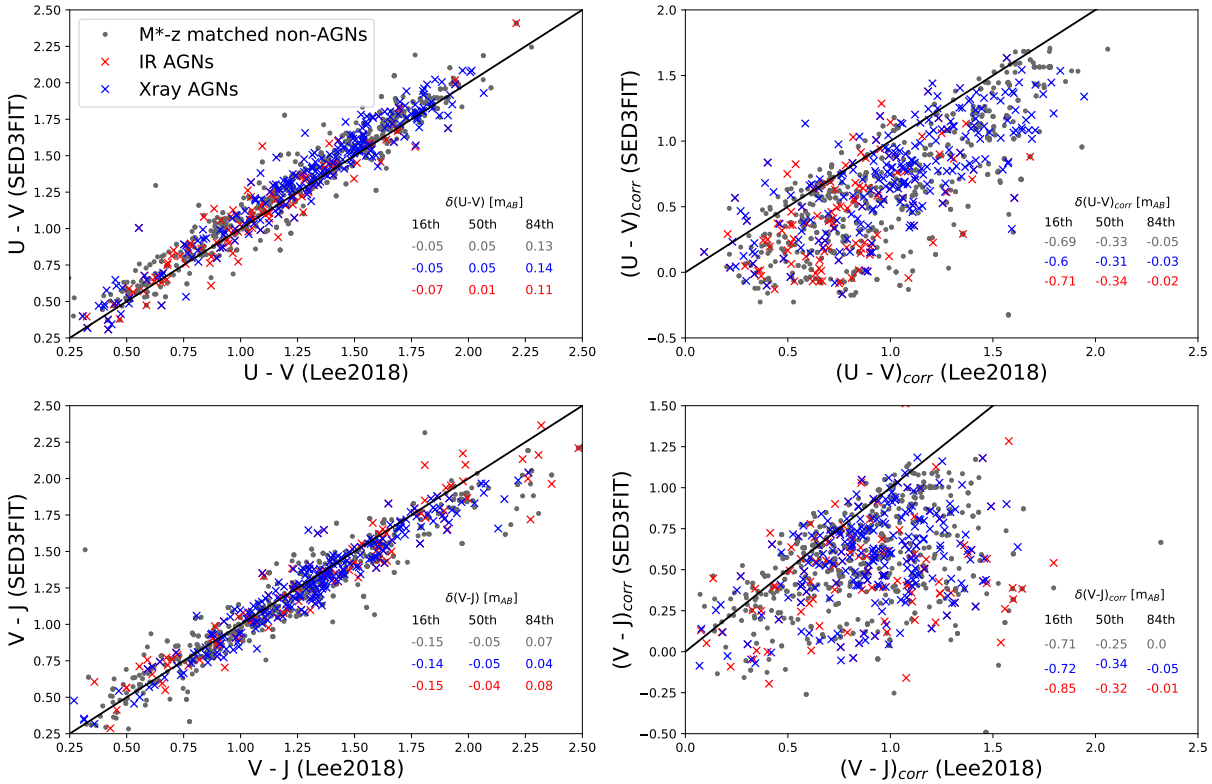

Figure 28. Comparisons of rest-frame colors derived by the two SED fitting procedures. **Left:** Comparisons between the apparent (i.e. dust-uncorrected) colors U−V and V−J. **Right:** Comparisons between the dust-corrected colors $(U - V)_{corr}$ and $(V - J)_{corr}$. Also tabulated in each panel are 16th, 50th and 84th percentiles of the corresponding differences between the two measurements for X-ray AGNs (blue), IR AGNs (red) and M_*-z matched non-AGNs (grey).

at MIR wavelengths, comparatively little is known about their SEDs at rest-frame UV/optical. If the adopted AGN templates considerably deviate from the true AGN spectral shapes in the UV/optical window, our tests on the optical colors will be biased.